DESIGN AND TESTING OF THE NAVIGATION MODEL FOR THREE AXIS STABILIZED EARTH ORIENTED SATELLITES APPLIED TO THE ATS-6 SATELLITE IMAGE DATA BASE

A REPORT

from the space science and engineering center
the university of wisconsin-madison
madison, wisconsin

DESIGN AND TESTING OF THE NAVIGATION MODEL FOR THREE AXIS STABILIZED EARTH ORIENTED SATELLITES APPLIED TO THE ATS-6 SATELLITE IMAGE DATA BASE

Progress Report for Period Ending 31 June 1976

Contract Number NAS5-20974

For

National Aeronautics and Space Administration
Goddard Space Flight Center
Greenbelt, Maryland 20771

By

W. W. Kuhlow
G. C. Chatters

University of Wisconsin
Space Science and Engineering Center
1225 West Dayton Street
Madison, Wisconsin 53706

June 1976

TABLE OF CONTENTS

I. INTRODUCTION

This report summarizes the work done thus far under Contract NAS5-20974 concerning development of the three axis stabilized navigation model and testing of the ATS-6 image data for the purpose of wind measurements.

There were two objectives to this phase of the work: to develop a methodology to deal with the ATS-6 attitude changes, and to develop the necessary software to generate from the ATS-6 image data cloud displacement measurements and wind data sets to be compared to those derived from the SMS-1 images (and model) covering the same time period. Both of these objectives have been met; however, the first requires some qualification.

Several unanticipated problems were encountered in relating the attitude telemetry data to the ATS-6 data images. These problems include oscillations in the element direction in one of the images, low frequency noise in the attitude telemetry data which was initially thought to represent real attitude changes, and other problems discussed in this report. However, gradually techniques were developed to partially compensate for them. We now believe that we have identified the key problem areas in which further work needs to be done to improve the accuracy of the model for wind measurements.

The ATS-6/SMS-1 comparison wind sets presented in this report represents first-effort results to measure ATS-6 winds. The results are quite good. Agreement between the two sets was best for low level trade cumuli. Quantitative comparisons were made at interpolated uniformly spaced grid points and for selected individual comparison clouds. In the southern half of the study area, the maximum magnitude of vector differences between ATS-6 and SMS-1 wind velocities was 2.5 meters per second with an average

difference of 1.5 m/sec. For these same vectors the differences in direction did not exceed 8°. The northern half of the study showed a systematic error around 3 m/sec in the northerly velocity component for the low level clouds. High level clouds were also tracked but since there were fewer comparison measurements and since reliable measurements are difficult to get for SMS as well as ATS, only plots of the high level winds are presented without any quantitative comparison.

II. ATS-6/SMS-1 CLOUD VELOCITY COMPARISON MEASUREMENTS

One of the most important uses of cloud images from geosynchronous satellites and one of the main goals of this contract work is the measurement of cloud velocities from a time sequence of images. For this report we have measured the cloud velocity wind field in an area of the western Atlantic Ocean where simultaneous ATS-6 and SMS-1 coverage was available. In this section we will describe what we learned from the wind set measurements, how they were obtained and our final results.

1. Background on the Comparison Wind Sets

Measurement of cloud velocity from sequences of images from spin scan satellites is a well developed process. The navigation model in use at SSEC for the SMS series is capable of aligning successive images to within one pixel (at 1 km resolution). Thus, SMS data is well suited for use in evaluating the capabilities of the ATS-6 image data and navigation model.

The area selected for this comparison wind set is characterized as follows: The area, of course, was visible from both the SMS-1 and ATS.6. (At this time the SMS subpoint was at 45° W longitude and the ATS-6 subpoint was at 90° W. The area selected was centered at 72° W longitude.) The weather in this area, centered at about 22° N latitude, was nearly the best that we could expect to find for this initial test. For this comparison, the area of primary interest is the wide zone of small trade cumulus covering most of the area south of a front which extends to the east of Florida (Figure II.1). These trade cumuli tend to be quite stable in their shape, and their flow patterns are uniform over a rather wide area. As a result

these clouds are some of the easiest to select and track. In addition there are cirrus clouds blowing off the top of convective cells in the front. This cloud type is one of the most difficult to track, and although we did attempt to track some of them, we have not worked with them enough to make meaningful wind comparisons. Another type of activity, not readily apparent on the photographs, are some high level clouds coming off the coast of Venezuela. They are fairly stable in shape and reasonably easy to track. All of the clouds tracked were over water. Past experience has shown that clouds over land are more difficult to track and in this case most of the clouds visible over land were stationary ones caused by orographic effects.

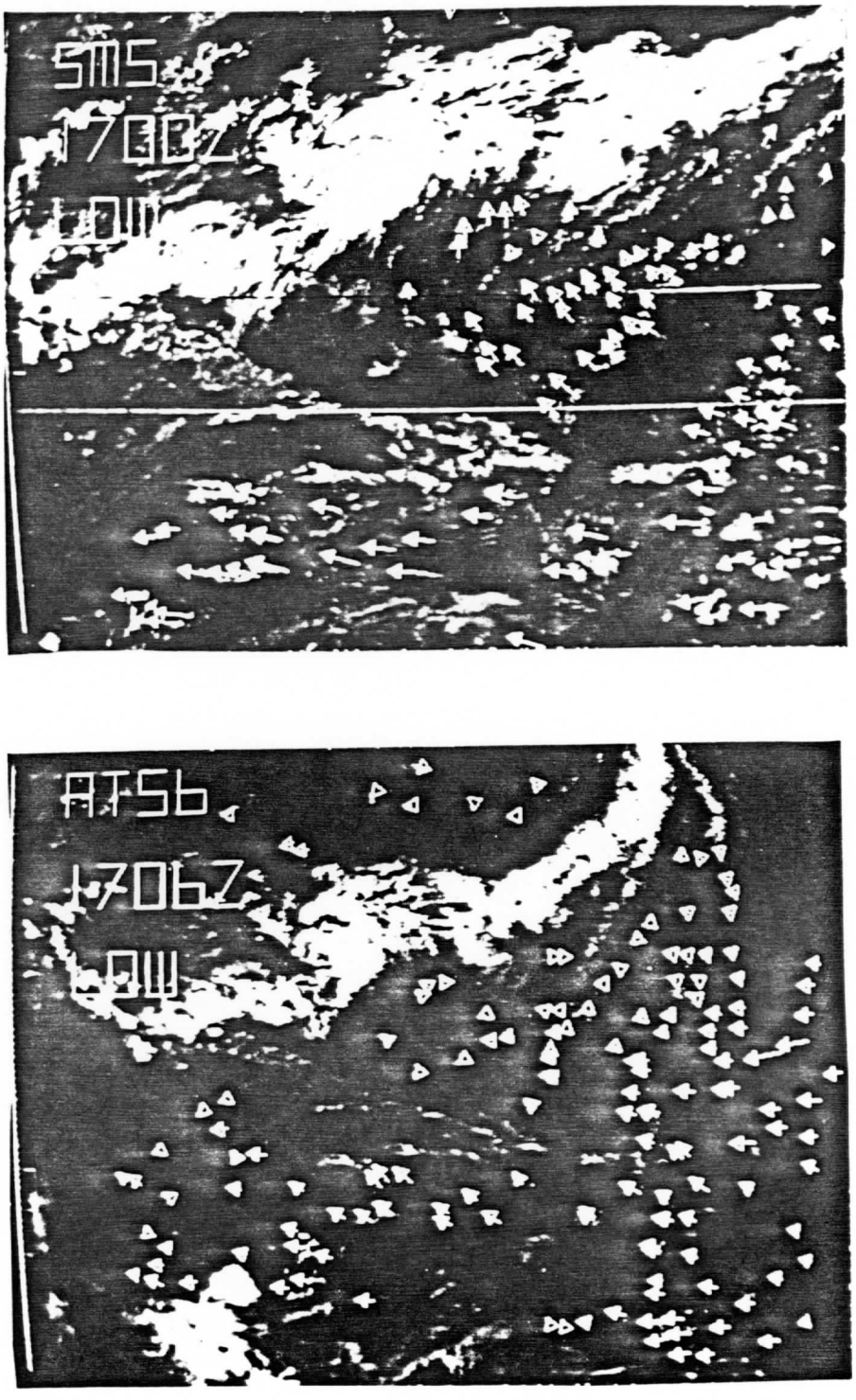

FIGURE II.1. Photographs of study area. The middle image of the three picture sequence shows the weather occurring in the study area. The upper image is from SMS-1. The most prominent landmark is Hispaniola just below the picture center. Cuba is visible to the northwest. The lower image shows the slightly larger area covered by the ATS-6 study area. The same landmarks are visible but at much lower contrast. Both images show the low level cloud velocity vectors computed between the second and third images.

2. General Procedures for Cloud Tracking

In this section we will briefly describe the procedures used in obtaining a wind set on the Man-computer Interactive Data Access System (McIDAS). The procedures used for spin scan satellites such as SMS have been well developed. The normal procedures were used for the SMS-1 wind set for this test. For the ATS-6 wind sets similar procedures were followed. Measuring cloud velocity involves five steps:

(1) Navigation

(2) Data staging and display

(3) Selection by cloud tracers

(4) Computation of cloud velocity

(5) Editing and correction.

Navigation is necessary for the staging and display of the SMS data. By "navigation" we refer to the process of establishing the parameters needed by the computer to transform satellite image coordinate (line, element) location to earth coordinate (latitude, longitude) locations. For SMS this requires entering the orbital elements, as supplied by NASA, into the computer; then the line-element position of a sequence of known landmarks is measured for use in computing satellite attitude. Beta count was used for the element direction alignment. The ATS-6 navigation was not needed for data staging.

The data staging is peculiar to the McIDAS. The McIDAS uses a standard broadcast television format for its display. 500 of the 525 lines are used on the display; each line is divided into 672 elements. The display is an analog device; the corresponding digital satellite data is stored on digital disk in an array of 500 rows by 672 columns.

For ATS-6 the digital data was read off of 9 track tape at full resolution. ATS-6 requires shifting of alternate scans since the east to west scans are not aligned with the west to east scans on the data tape. A shift which aligned the center of the image was used for all wind measurements. Later tests showed that scan misalignment in off-center regions had only a small effect on cloud displacement computations. McIDAS only handles up to 8 bit data so the least significant bit of the ATS-6 9 bit data was dropped. For SMS-1 the digital data were retrieved from slant track tape from the full resolution archive of GATE data. The data were reduced in resolution by a factor of four; elements were averaged in groups of four and data were taken only from every fourth line.

Even at this reduced resolution the SMS-1 data still had finer resolution than the ATS-6. The SMS-1 image sequence covered an area from about 13° N to 32° N latitude and from 85° W to 61° W longitude. The ATS-6 sequence covered a slightly larger area. Since the ATS-6 attitude control attempts to keep the equatorial region of the earth fixed relative to its field of view we only had to use the same image coordinate load points for each of the three images to produce a reasonably well aligned image sequence.

In an interactive system like McIDAS, cloud tracers are selected by an operator while viewing the sequence of cloud images on the TV display. In the usual procedure for cloud tracking, the operator starts out by stepping through the sequence of images several times to get an overall idea of the flow patterns. The flow is visually divided into various height levels. For SMS-1 data the flow patterns, infrared images and a cloud height computation program were used to aid in defining the levels

of the various flow patterns. So far we have not used the ATS-6 infrared data for height determination. For most of the work on this comparison wind set, only two cloud levels were used: low, for the trade cumulus at around 800 mb; and high, for the cirrus generally around 200 mb.

Once a cloud was selected in each of two images, the computer computes displacement in image coordinates using a correlation method. Typically, a 20 x 20 array of data is read from the digital image array of the first image in the sequence. Correlations are computed for lags of $\pm$ 3 pixels from the center of a 26 x 26 array read from the second image in the sequence. The numbers used here are typical values; all may be varied by the operator.

After the cloud displacement in image coordinates has been computed, the navigation program was used to convert them to earth coordinates from which the cloud velocity is computed. At this stage, the processing for ATS-6 and SMS was slightly different. Since the SMS navigation was operating on McIDAS, the wind computation could be done immediately and the operator could view the results continuously. On the other hand, ATS-6 winds were computed on the Univac 1110, so the results of the computation could not be seen for a couple of days. The end results were basically the same, except that the operator did not have the feedback provided by immediate wind computation. However, image coordinate winds were plotted and printed to give some immediate indication of the success of the cloud selection process.

The last step was editing and correction. A graphics display system on McIDAS plots wind vectors over the cloud tracers on the TV display. Frequently, a few vectors are bad enough to warrant deletion from the set. These are usually vectors that are pointed in the wrong direction for the apparent cloud motion or do not conform to the general flow pattern and were based on rather doubtful tracers. The final wind sets are plotted as shown in the next subsection.

3. The Resulting Wind Fields

The resulting wind fields are presented here in several forms. The photographs of Section II-2 show the weather activity occurring at the time. For each cloud, two vectors were averaged for the graphic presentations shown here. The individual wind measurements are shown in FIGURES 2 through 5. Each level for each satellite is on a separate plot. These raw wind measurements were then input to an objective analysis program (developed at the Stanford Research Institute) to generate wind vectors at uniformly spaced grid points. These plots also are done for each level for each satellite and are presented in FIGURES 6 through 9. In all of these plots the length of the vector is proportional to its velocity. A 10 m/sec scale vector is shown in the lower left corner of FIGURES 6 through 9. The scale is the same for all the plots. In addition to the plots, two tables are given. One shows the velocities of several selected low level clouds, each of which was measured from both ATS-6 and SMS-1 images. (TABLE II.1); the other shows the vector values and differences at those grid points where both SMS and ATS-6 had a value (TABLE II.2).

For our present purposes the low level winds are of primary interest. In the SMS wind plot we see an area of mostly easterly trade winds in the southern and eastern parts of the study area. Near the middle of the plots, especially north of Hispaniola, the trades curve anticyclonically to converge into the front that lies east of Florida. Since there are many cloud tracers in this region and the wind field is quite uniform, this area will be our first point of comparison. Looking at the ATS-6 plot of low level winds we see a quite similar pattern. Because of the resolution mismatch, ATS-6 covers a slightly greater geographic area. The region

south of 20° N latitude shows especially good agreement. Looking at TABLE II.1 and II.2 we see that the largest magnitude of the vector differences is less than 2.5 m/sec, and the differences in direction are less than 8° maximum. North of 20° N the general patterns are similar but there is apparently a systematic error in the V (northward) component of the velocity. The tables confirm this and indicate that the magnitude of this error is about 3 m/sec. The suspected cause of this error is an ATS-6 roll change which was not properly accounted for. This is discussed in the following sections.

Some low level clouds north of the front were tracked but form a rather random pattern and are useless for comparison. The high level winds, associated with the front, lack the widespread uniformity of the low level winds and are difficult to compare precisely. (On the other hand, cirrus coming off Venezuela at about 15° N, 70° W was picked up by both satellites and shows general agreement.) Along the front a region of northeastward flow is picked up east of 70° W. West of 70° W the pattern becomes somewhat random but shows some indication of divergence as would be expected from the large convective cells along the front.

In summary, we can say the following:

(1) Good wind vectors can be obtained from ATS-6 as shown by the low level vectors south of 20° N, where the magnitude of vector difference is less than 2.5 m/sec and differences in direction are less than 8° maximum.

(2) There are errors in the navigation system which caused systematic errors in velocity computations north of 20° N in the study area. These errors were approximately 3 m/sec in the V (northward) component.

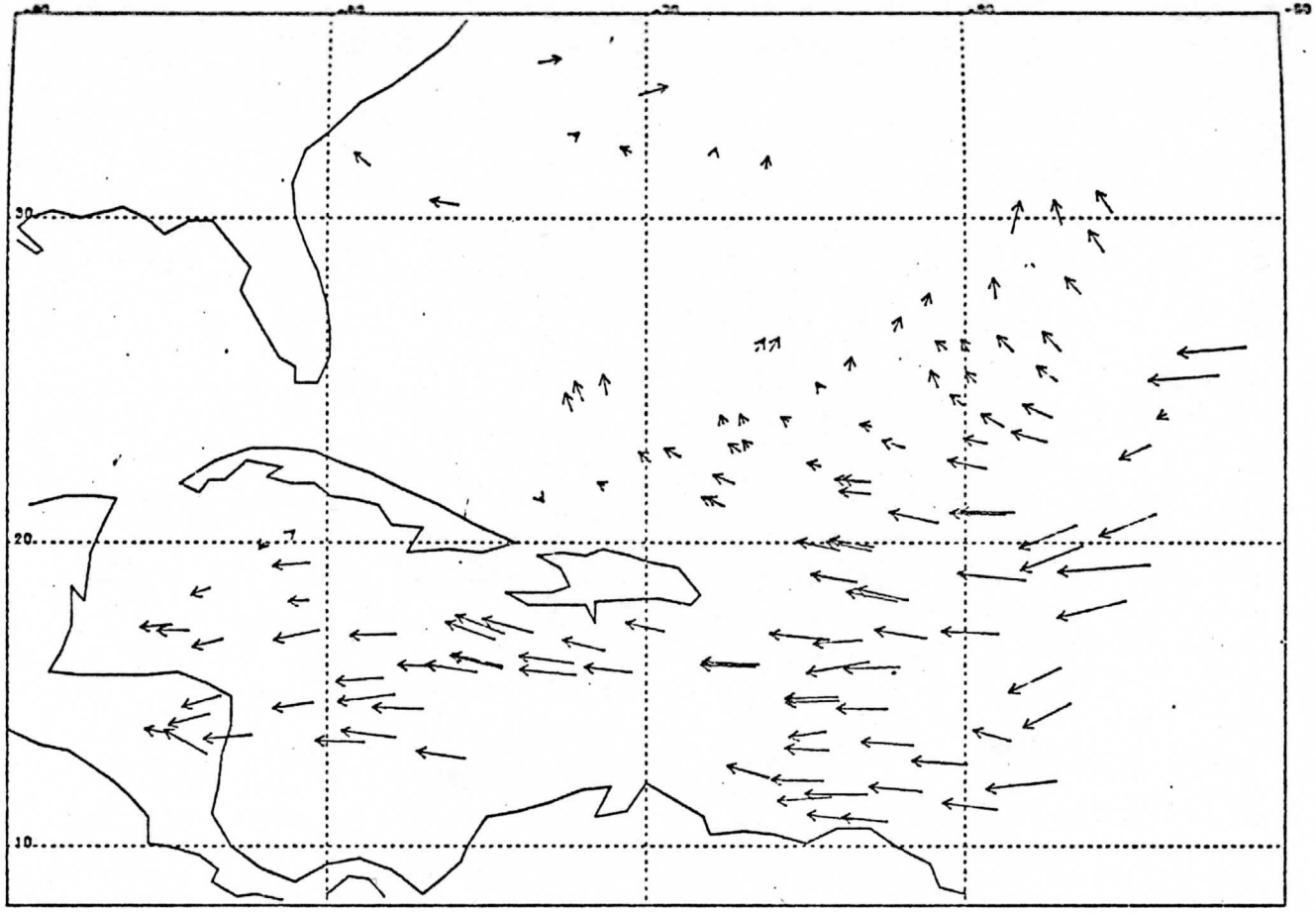

FIGURE II.2. Low level winds from ATS-6. Length of the vector is proportional to velocity. South of 20°N the easterly flow is quite uniform. North of 20°N the flow curves to converge on the front. Comparing the region from 20°N to 10°N with the SMS-1 vectors clearly shows the systematic error in the V (northward) component of velocity.

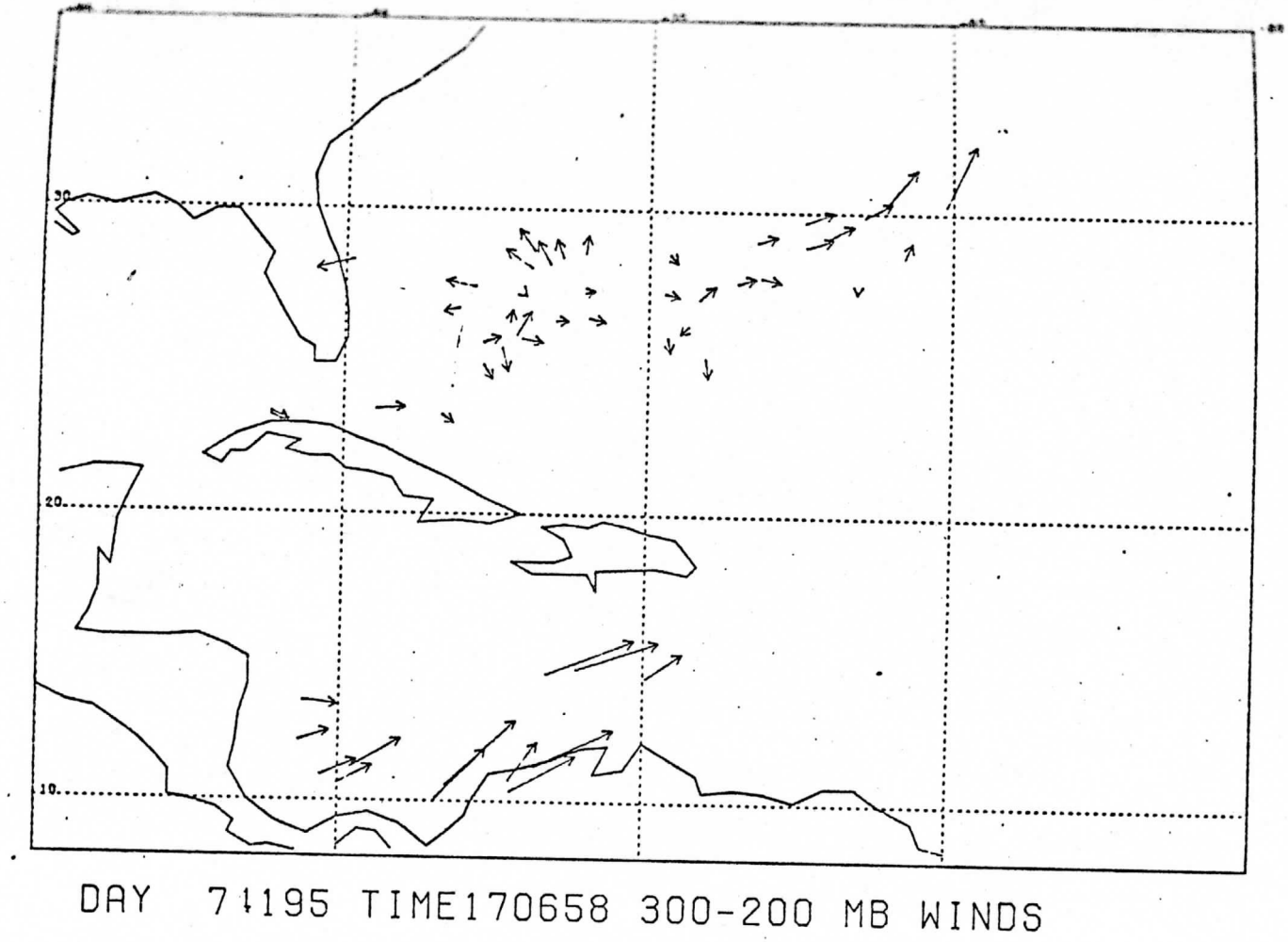

FIGURE II.3. High level winds from ATS-6. North of 20°N the winds are associated with cirrus blowing off the tops of convective cells in the front. East of 70°W longitude there is organization in a southwesterly flow; west of 70°W the pattern is a bit more random but shows some divergence from individual cells. South of 20°N the winds are associated with some thin high level clouds which were not immediately related to convective activity.

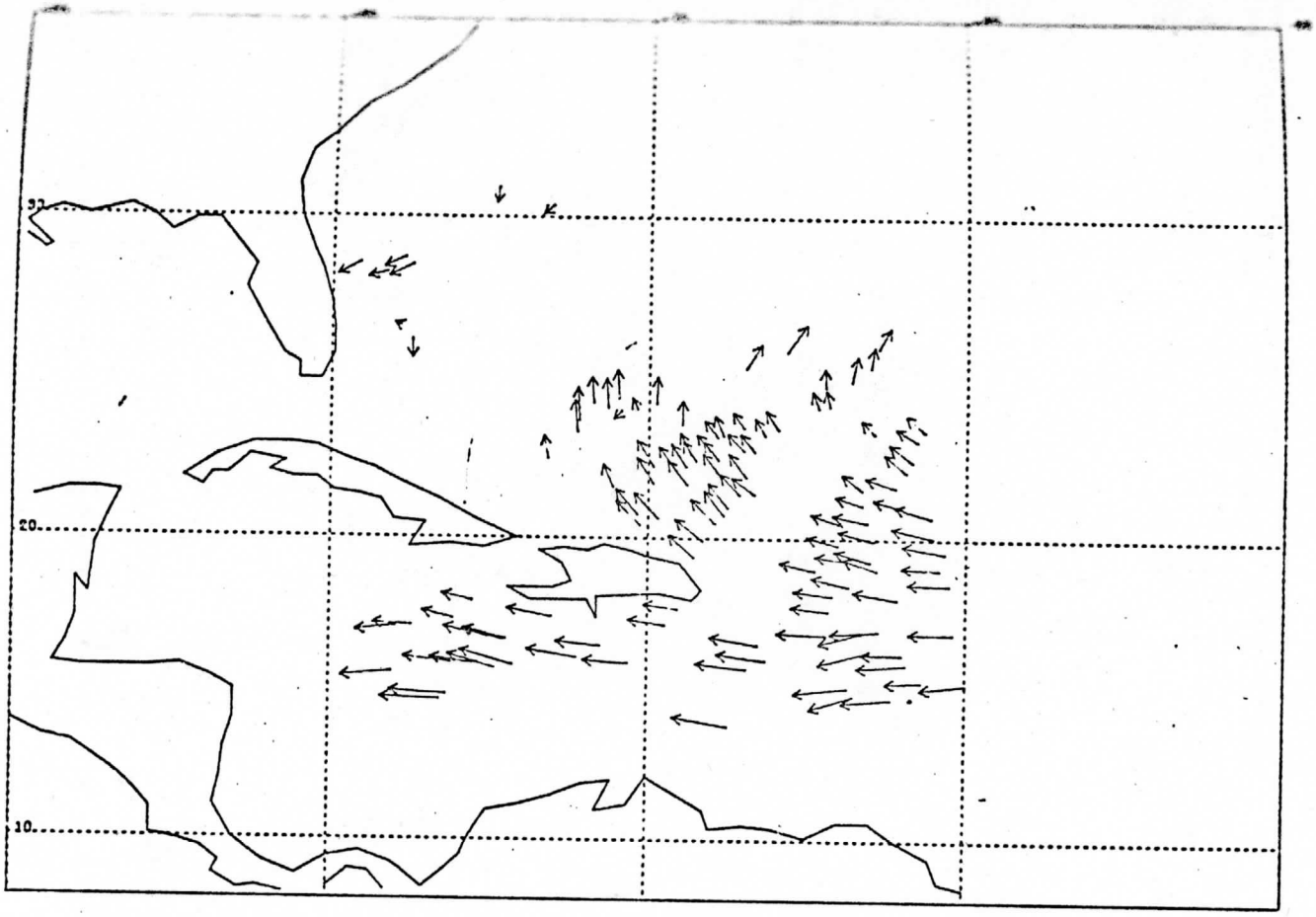

FIGURE II.4. Low level winds from SMS. Compare to FIGURE II.2 the ATS-6 winds. The field is quite smoothly varying to the south of the front. To the north of the front a few low clouds were tracked but not enough were found to see any general pattern to the flow in that region.

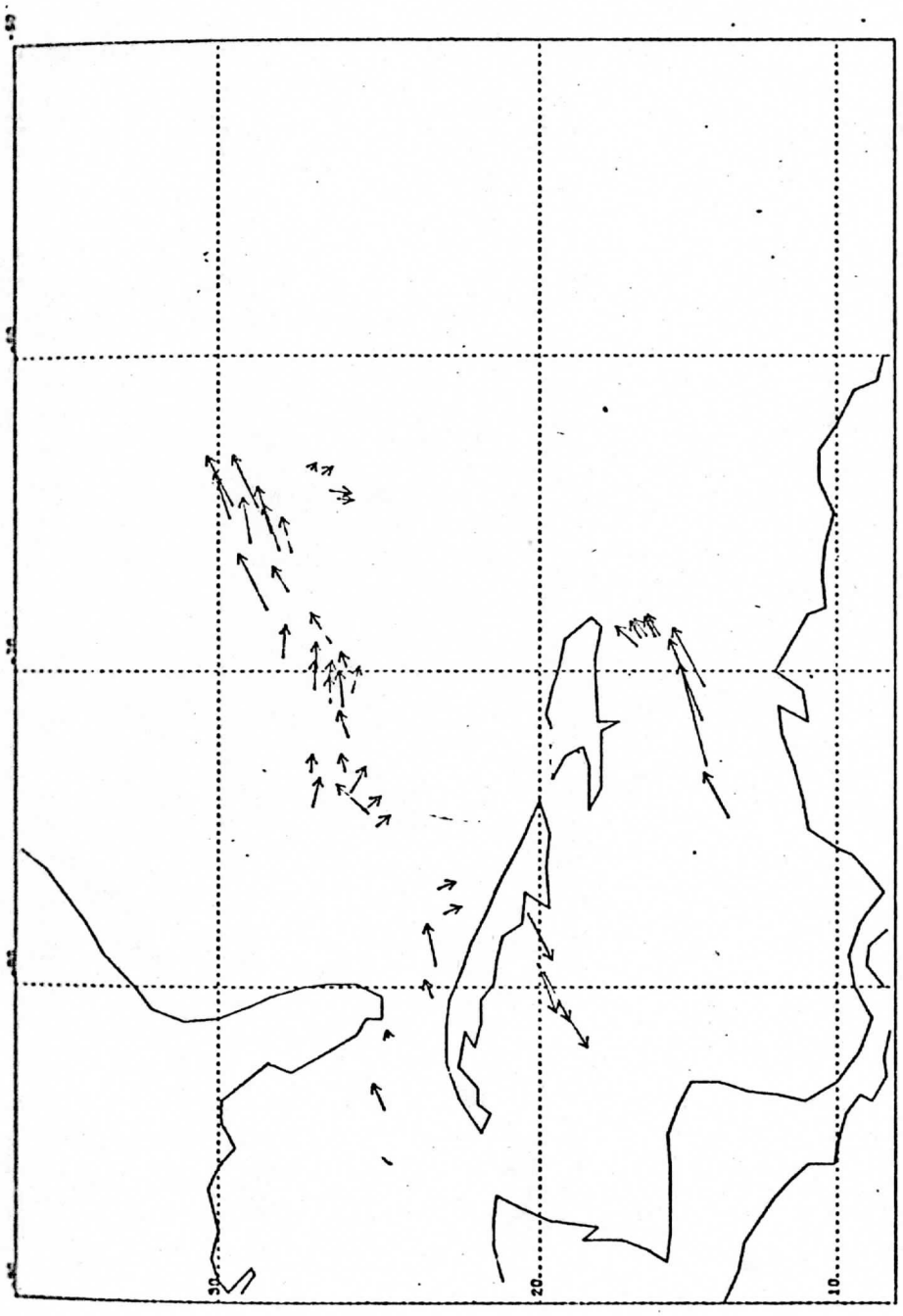

FIGURE II.5. High level winds from SMS-1. The patterns are similar to the ATS-6 measurements.

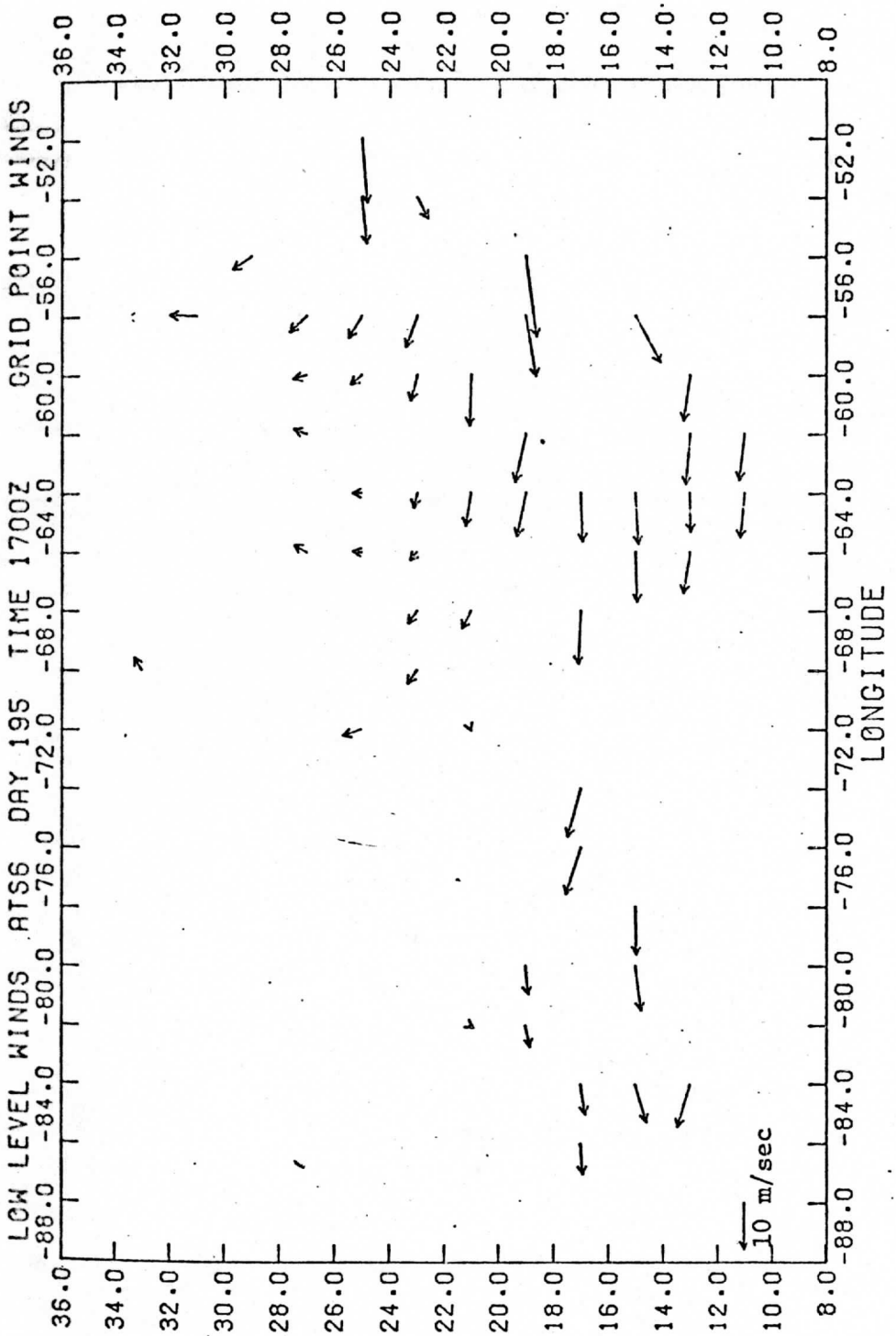

FIGURE II.6. Uniform grid of low level winds from ATS-6. These wind vectors are interpolated to 2° latitude and longitude grid points from the data shown in FIGURE II.2. The same patterns as seen in FIGURE II.2 are evident. Where a grid point vector was computed for both ATS-6 and SMS-1, it is listed in TABLE II.2. A 10 m/sec reference vector is shown in the lower left-hand corner.

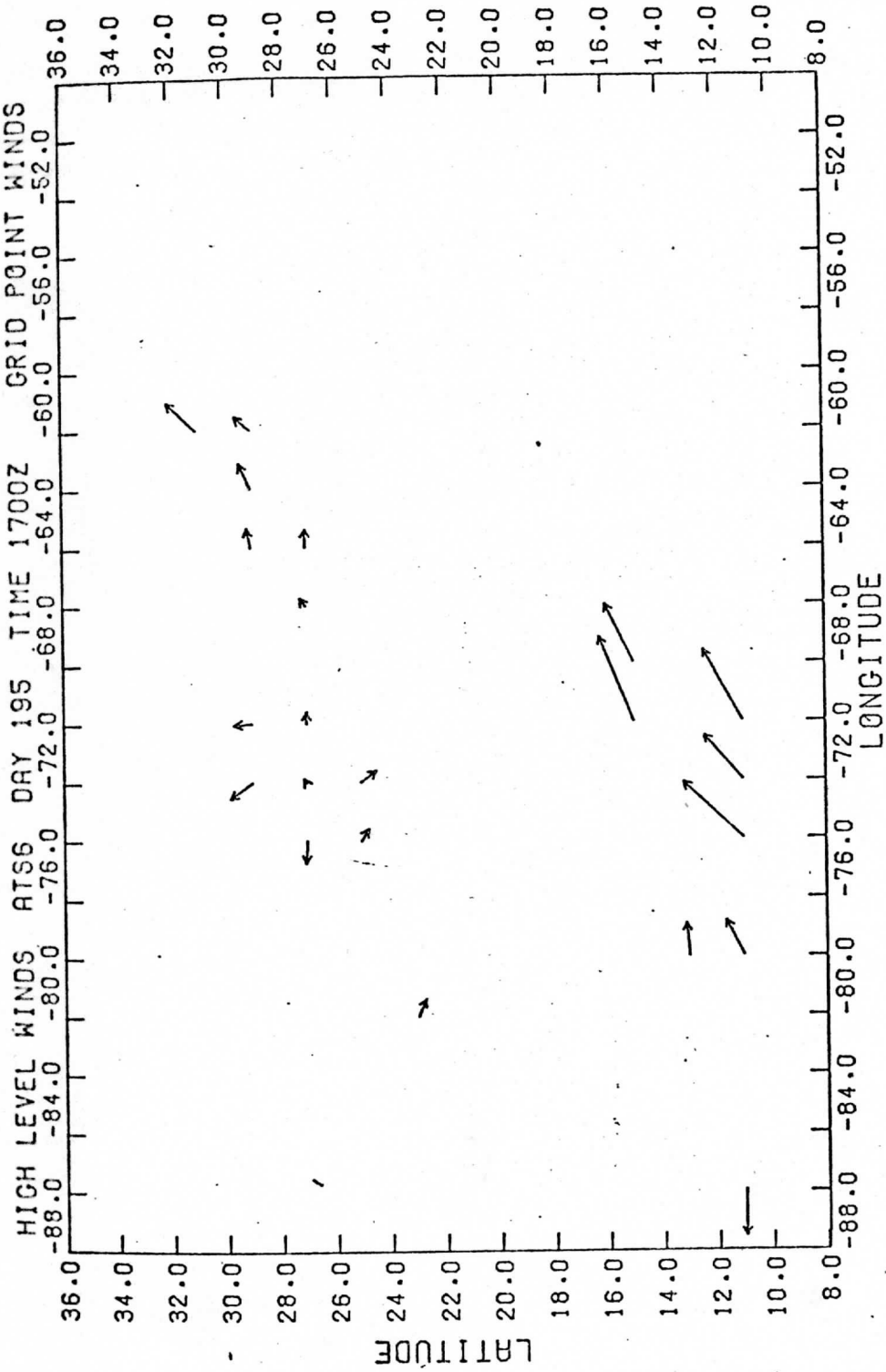

FIGURE II.7. Uniform grid of high level winds from ATS-6. These vectors were computed in the same manner used for the plot in FIGURE II.6. A reference vector of 10 m/sec is printed at 11°N, -88°W.

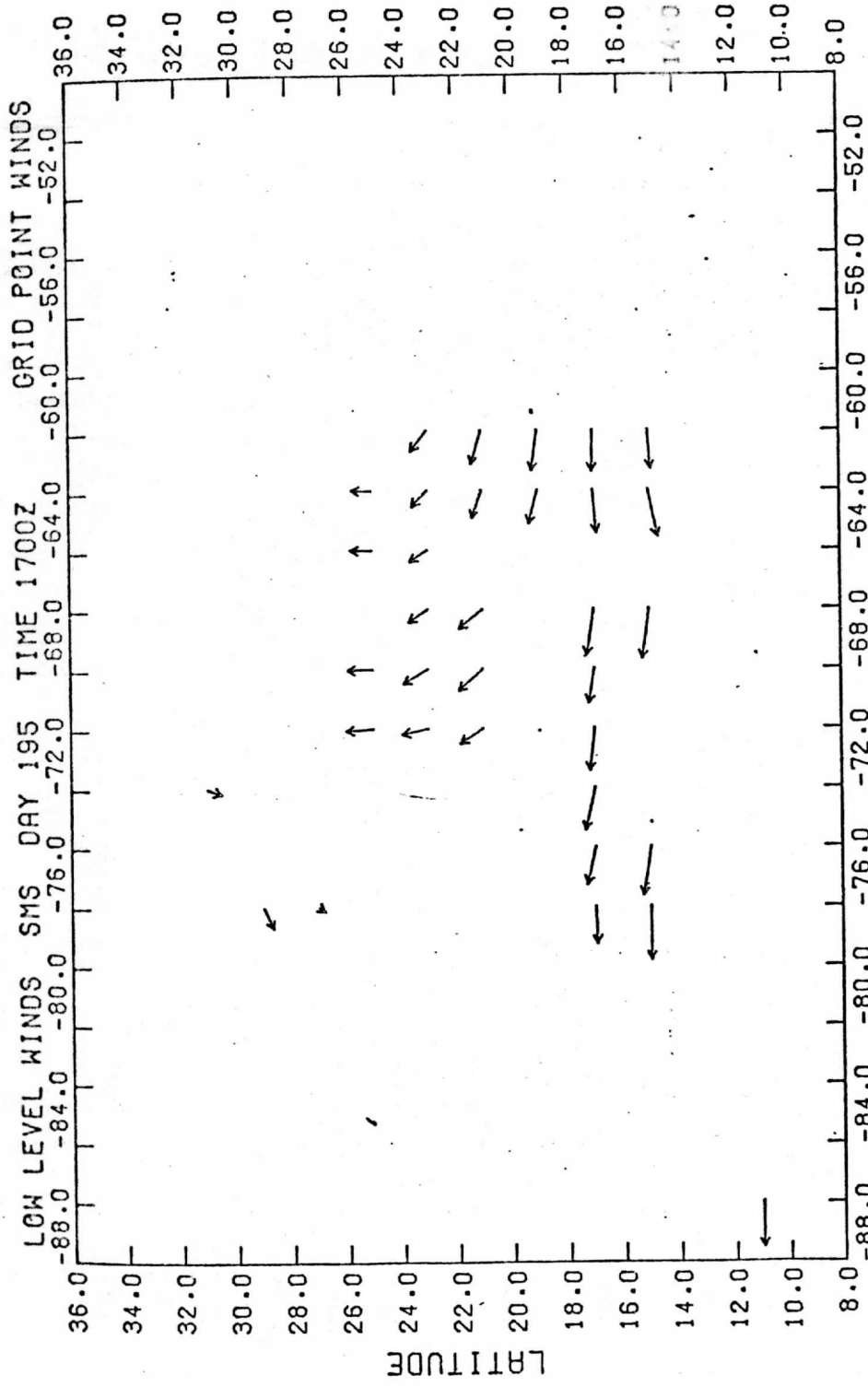

FIGURE II.8. Uniform grid of low level winds from SMS-1. A 10 m/sec reference vector is shown in the lower left-hand corner of the plot.

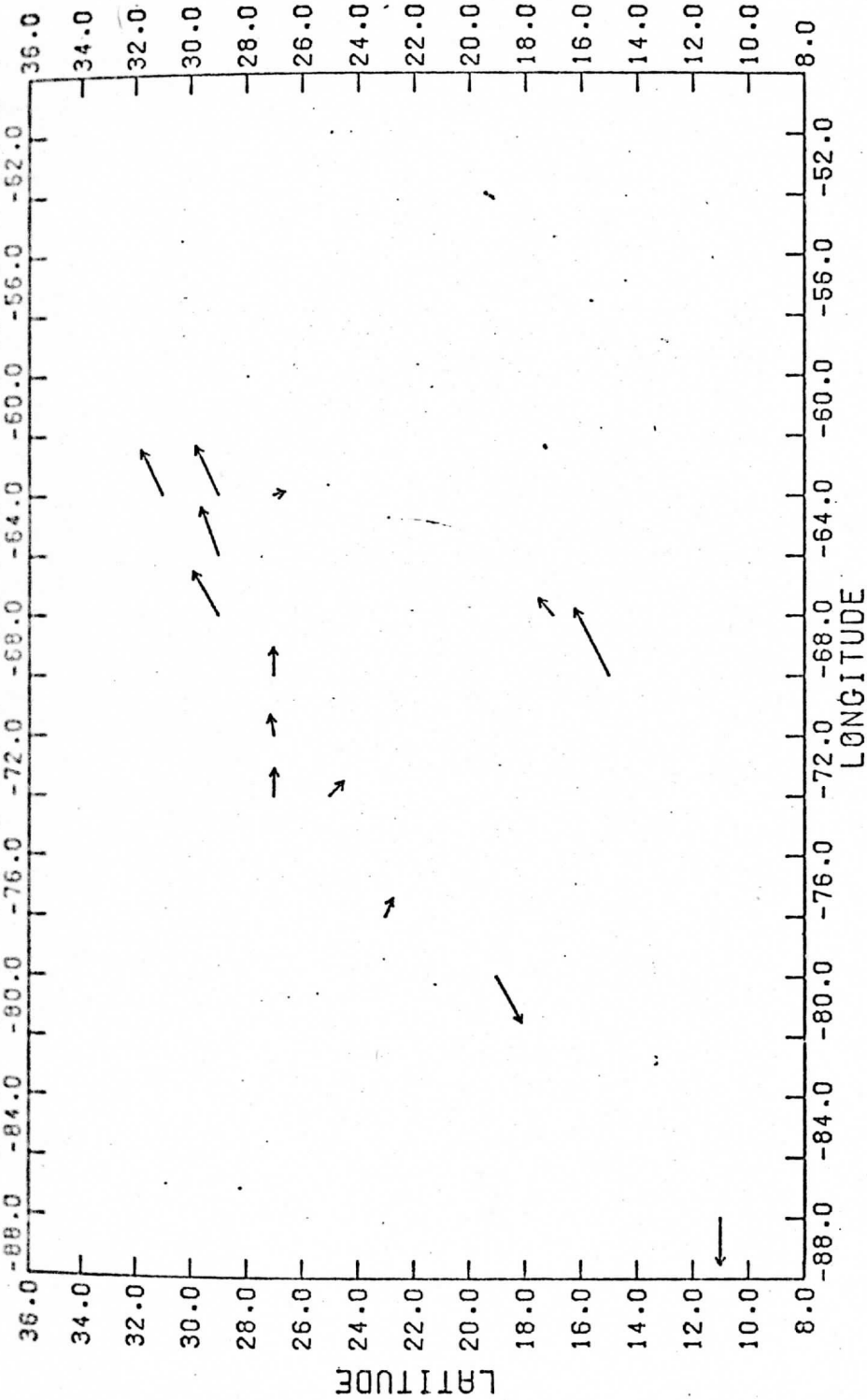

FIGURE II.9. Uniform grid of high level winds from SMS-1. Parts of the pattern agree with ATS-6 but quite a few discrepancies still exist. At this point in the development of the system no conclusion can be drawn from any differences in the high level winds. The problems evident in the low levels (FIGURES II.6, II.8) will have to be resolved before any useful studies can be done on the high level winds. A 10 m/sec reference vector is shown in the lower left-hand corner of the plot.

ATS6/SMS1 POINT COMPARISON CLOUDS

VALUES AND DIFFERENCES

		SMS		ATS-6		DIFFERENCE			
LAT	LON	U	V	U	V	U	V	$\lvert\vec{V}_S-\vec{V}_A\rvert$	$\Delta\phi$
22.99	-66.75	- 2.82	4.25	- 1.25	1.33	-1.57	2.92	3.32	-10°
21.75	-67.48	- 4.14	5.27	- 4.29	1.65	.15	3.62	3.62	-31°
21.12	-67.76	- 3.99	5.15	- 3.50	1.87	- .49	3.28	3.32	-24°
20.10	-63.46	- 7.45	2.51	- 8.96	1.65	1.51	.86	1.74	- 8°
18.21	-62.81	- 9.14	2.31	-10.38	2.23	1.24	.08	1.24	- 2°
16.10	-74.88	-10.95	3.76	-10.52	2.82	- .43	.94	1.03	- 4°
16.05	-67.13	-11.22	1.36	-11.67	.66	.45	.70	.83	- 4°
15.97	-63.84	-11.00	-2.28	-12.70	-2.44	-1.70	.16	1.71	1°
15.17	-64.34	-11.16	-1.44	-10.76	- .41	- .40	-1.03	1.10	5°

TABLE II.1. Winds for nine low level clouds which could be identified on both the SMS-1 and ATS-6 images are listed. U and V components are given for measurements on each satellite. Differences in U and V components, magnitude of vector difference and difference in direction ($\Delta\phi$) are given.

SMS-ATS DIFFERENCES AT GRID POINTS

		SMS		ATS-6		DIFFERENCE			
LAT	LON	U	V	U	V	U	V	$\lvert\vec{V}_S-\vec{V}_A\rvert$	$\Delta\phi$
-72	25	- .36	5.80	- 1.30	3.77	+ .94	2.03	2.24	-15°
-66	25	.07	4.52	.28	1.78	- .21	2.74	2.75	+ 8°
-64	25	.10	4.26	- .06	1.82	.16	2.44	2.45	- 3°
-70	23	- 3.09	5.18	- 2.79	1.81	- .30	3.37	3.38	-26°
-68	23	- 2.67	3.89	- 2.57	1.69	- .10	2.20	2.20	-22°
-66	23	- 2.46	3.72	- 1.60	1.31	- .86	2.41	2.56	-17°
-64	23	- 3.40	3.12	- 3.05	.58	- .35	2.54	2.56	-32
-72	21	- 3.15	4.94	- .26	-.10	-2.89	5.04	5.81	-79
-68	21	- 4.16	5.00	- 3.74	1.99	- .42	3.01	3.04	-22
-64	21	- 5.93	2.13	- 7.10	1.19	1.17	.94	1.50	-10
-64	19	- 7.21	1.83	- 9.32	1.93	2.11	- .10	2.11	- 3
-62	19	- 8.56	1.15	-10.33	2.33	1.77	-1.18	2.13	+ 5°
-76	17	- 8.06	1.79	-10.00	3.28	1.94	-1.49	2.45	+ 6°
-74	17	- 9.15	2.08	-10.38	2.79	1.23	- .71	1.42	+ 2°
-68	17	-10.02	1.58	-11.46	.56	1.44	1.02	1.76	- 6°
-64	17	- 9.25	-.79	-10.45	-.36	1.20	- .43	1.27	+ 3°
-78	15	-11.60	-.06	-10.25	-.23	-1.35	.17	1.36	- 1°

TABLE II.2. Difference between ATS-6 and SMS-1 where common grid points on the SRI uniform grid plots both had a vector. Difference in U (eastward) and V (northward) velocity components are given as well as magnitude of vector differences and direction difference. Velocities are in meters per second.

III. CHARACTERISTICS OF ATS-6 IMAGE DATA AND ATTITUDE TELEMETRY DATA

This section summarizes the salient characteristics of the ATS-6 image data and the associated attitude telemetry data which have to be considered in the ATS-6 navigation/wind measurement model.

1. Mirror Scan Nonlinearities

ATS-6 digital imagery is recorded for both mirror scan directions and the deviations from a linear scan as a function of mirror sweep position are different for each direction (although the deviations repeat in magnitude and phase from line to line for the same sweep direction). The deviations of the odd relative to the even scan lines were measured by decomposing the ATS-6 image into two images, each composed of lines for the same sweep direction, and using an image matching technique to measure the relative deviations (in ATS-6 elements) as a function of element position along an arbitrary sweep line. The resulting curve fit to these measurements are accurate to better than one-half ATS-6 element deviation. The curve for the three DAY-195 images used in the wind measurement study appears in FIGURE III.1. (Although this curve is identical for these three images taken in succession (over a 75 minute period), they are in general different for data recorded on different days (ATS-6 NAVIGATION INTERIM REPORT, 11 June, 1975)).

In an operational mode where the data images are to be studied on a computer/video interactive display system such as McIDAS, the relative shift curve shown in FIGURE III.1 is used to predict the amount of shift necessary to translate the alternate sweep lines by a constant amount so

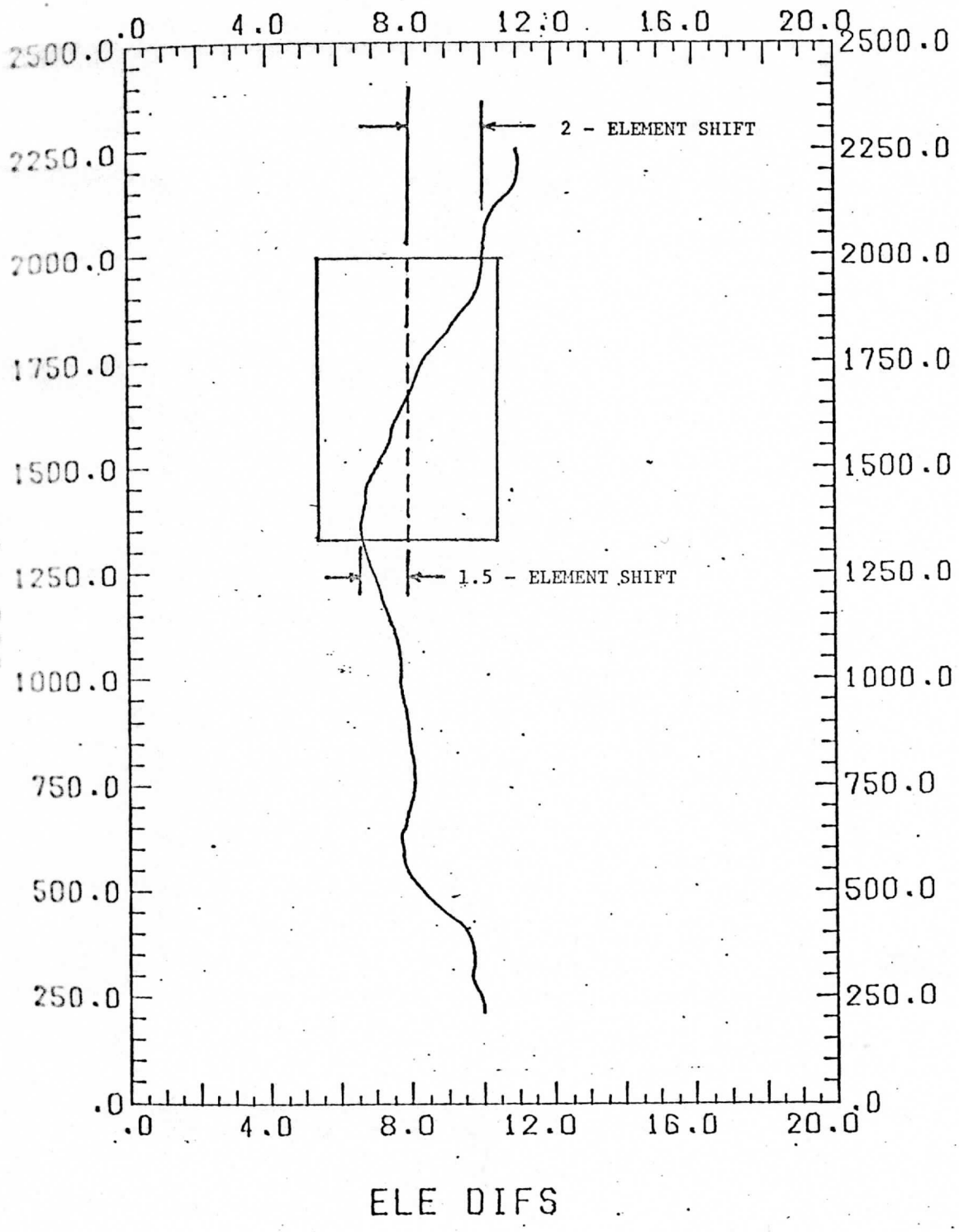

FIGURE III.1. Mirror Scan Nonlinearity Curve - DAY 195. Curve shows the shift in ATS-6 elements (ELE DIFS) of the odd relative to the even mirror scan line as a function of element position (ELE NUM) along an arbitrary scan line. Height of the box shows the element range of the study area.

that there is zero relative element shift close to the center of the viewed image. As implied by the figure, an 8-element shift was the value used for the three study area images. Also shown in the figure is the ATS-6 element range (672 elements to be McIDAS display compatible) associated with the study area. It is seen that there is a 1 1/2 to 2 element relative offset at the edges. This offset at the edges gives a waffled appearance to the clouds as the images are viewed on the McIDAS TV display but does not distort them beyond recognition for the purposes of wind measurements.

Since the image matching technique used for cloud displacement measurements does not automatically account for these element offsets, a small investigation was made to determine their effect on the accuracy of these measurements. The procedure for doing this and the results are discussed in Section V of this report. The conclusion is reached that the effect, if, indeed, there is any, of element offsets between alternate scan lines on cloud displacement measurements is small compared to errors caused by uncertainties in the attitude.

In concluding this subsection it is worth emphasizing that what we have been discussing was the effect of relative mirror scan nonlinearities and how they affect image measurements. There still remains the problem of absolute mirror scan nonlinearities, i.e. if we made an image by remapping the odd scan lines relative to the even in a manner implied by FIGURE III.1, would we have an earth image that was geometrically precise? Probably not. The amplitude of the wiggles of the relative element shift curve suggest that the absolute distortions would be on the order of one to two elements. There is no easy way to account for this. These distortions, if present,

would affect absolute navigation (prediction of the location of a cloud in earth coordinates) but would have negligible effects on wind measurements since the measured displacements of clouds are small compared to the distances over which such nonlinearities occur (one element shift over a 300 element scan range).

Attitude Telemetry Data

FIGURES III.2, III.3, and III.4 are plots of ATS-6 yaw, roll, and pitch attitude telemetry time series associated with the three images used in the ATS/SMS study. Note that the data for each plot covers all three images; the time of day is given in decimal minutes, GMT. The values were obtained directly from the ATS-6 magnetic data tapes supplied to us by NASA/GODDARD.

The times at which the wind field study area was imaged is delineated on each plot. Also shown on the roll and pitch figures is a vertical bar which denotes the change in angle (0.024 degrees) necessary to produce a 10 meter per second apparent motion at the subsatellite point over a two-image sequence (24.6 minutes). For the roll plot this change in angle would result in a 10 m/s v-component error; for the pitch, a 10 m/s u-component error.

What we have learned about this data is summarized here and discussed in more detail in the following subsections.

(1) The sawtooth curve appearing in the pitch and yaw plots is ficticious; in any of the testing procedures we have devised, we have not observed the slightest indication that the satellite was yawing and pitching

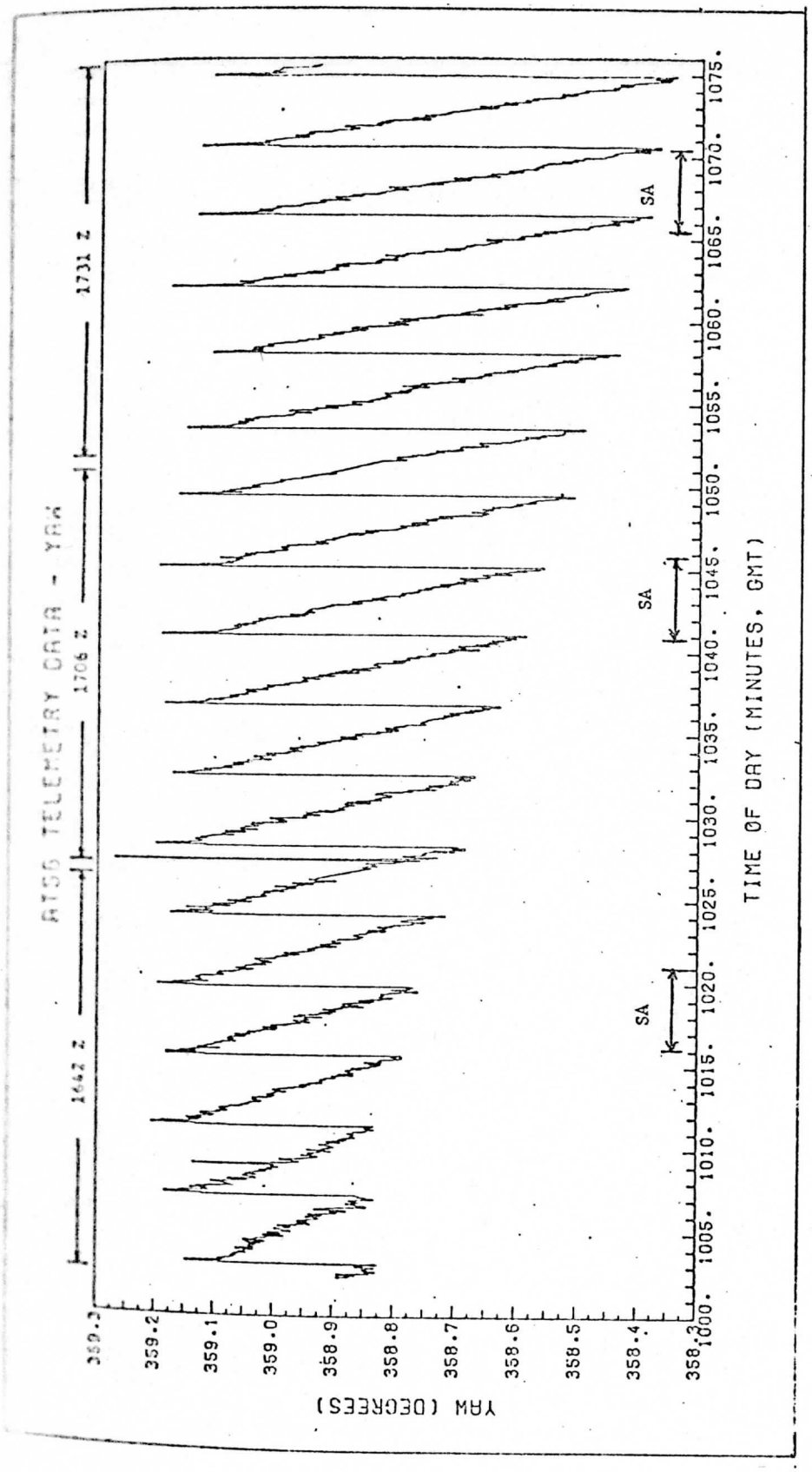

FIGURE III.2. ATS-6 Yaw Attitude Telemetry Time Series for Data Images 1642Z, 1706Z and 1731Z, DAY 195. The times at which the wind field study area was imaged is denoted by SA. The true yaw at the time these data were imaged (determined by methods discussed in this report) was much more stable than suggested by the telemetry data plot above.

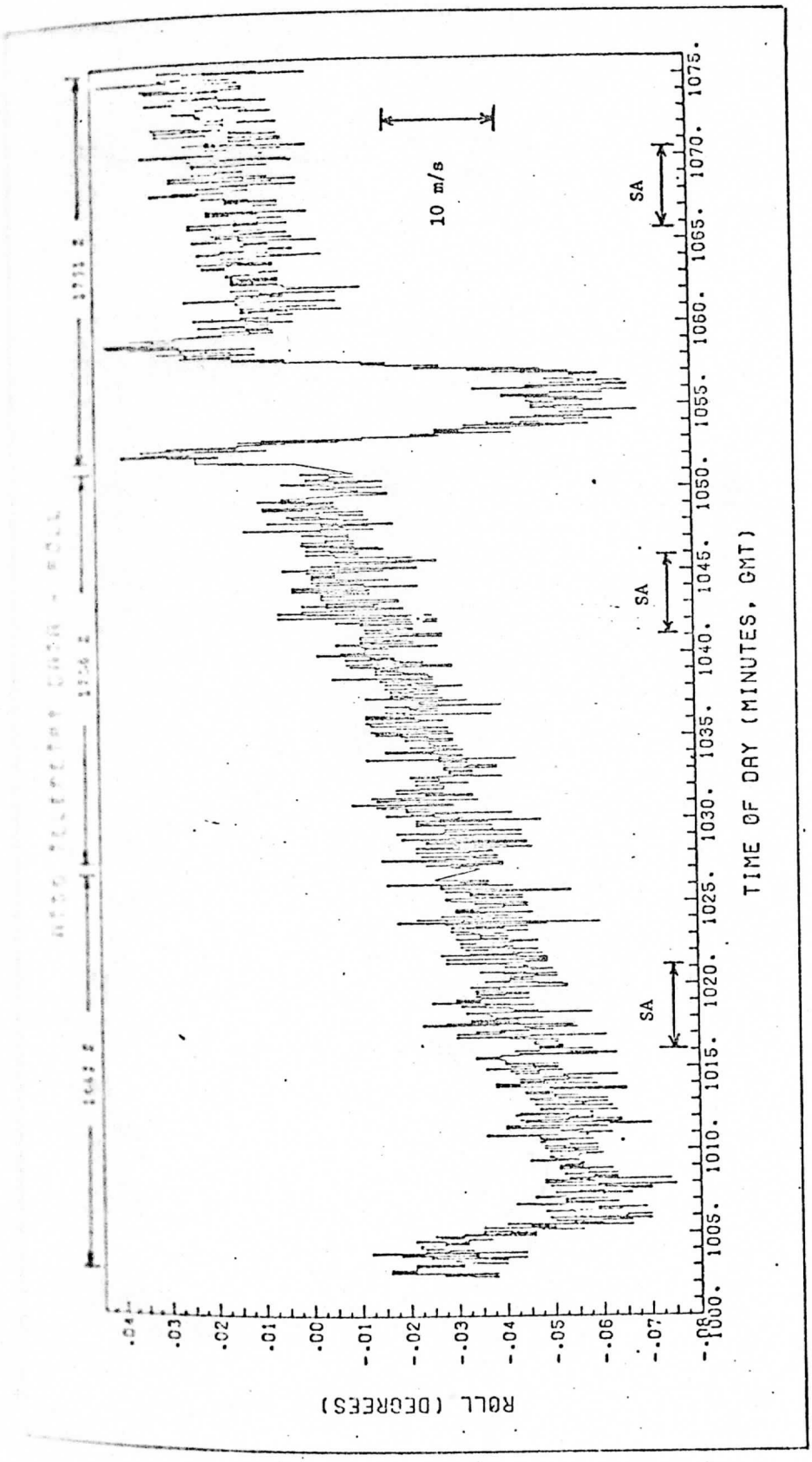

FIGURE III.3. ATS-6 Roll Attitude Telemetry Time Series for Data Images 1642Z, 1706Z, and 1731Z, DAY 195. The times at which the wind field study area was imaged is denoted by SA. The vertical bar denotes the change in roll angle (0.024°) necessary to produce a 10 meter per second apparent motion (in a north-south direction) at the subsatellite point over a two-image sequence (24.6 minutes). The large dip occurring at 1055 minutes GMT is accurately representative of the true roll angle change at that time (this was verified by methods discussed in this report). In general the roll attitude telemetry data is quite good.

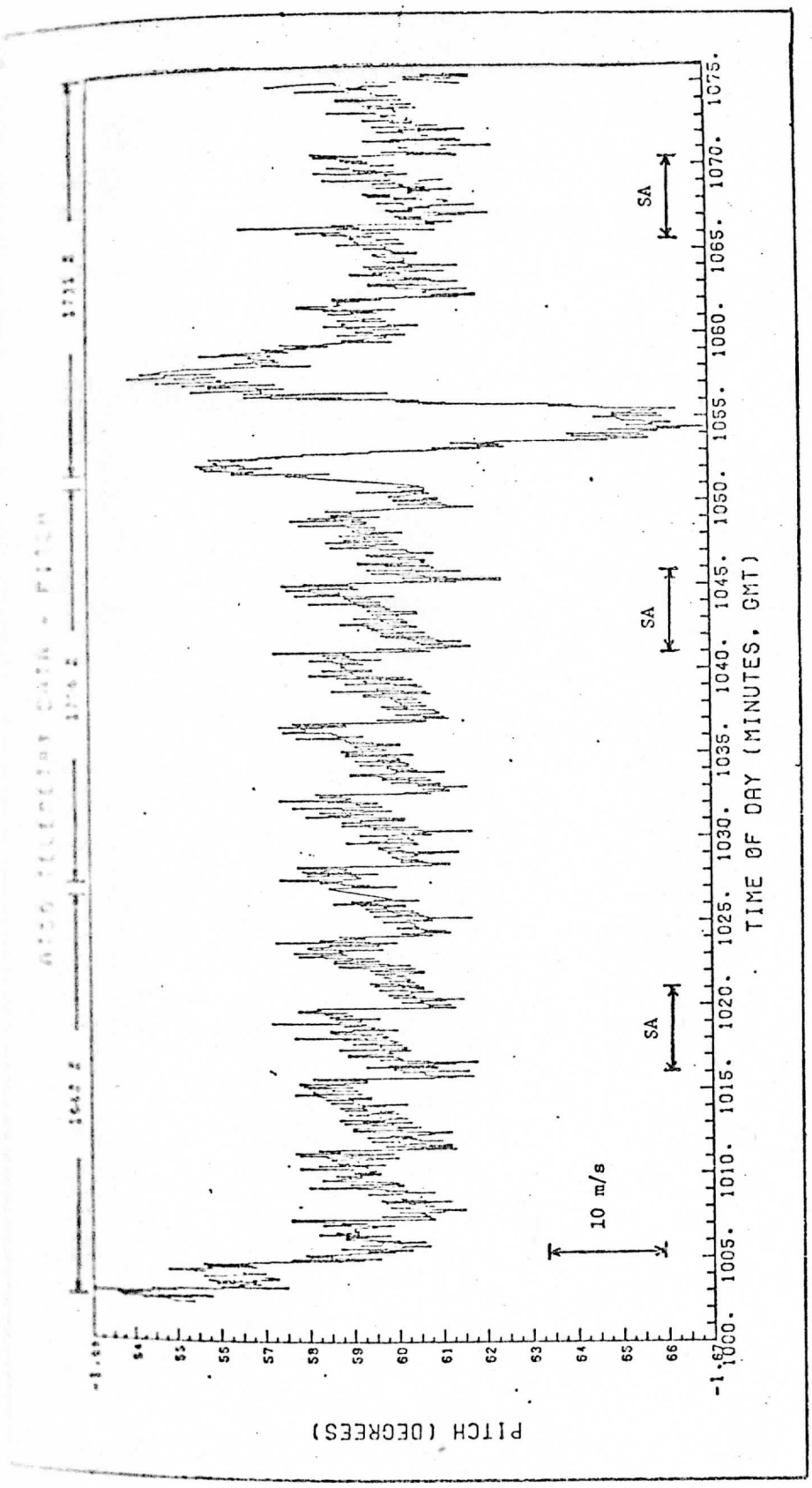

FIGURE III.4. ATS-6 Pitch Attitude Telemetry Time Series for Data Images 1642Z, 1706Z, and 1731Z, DAY 195. The times at which the wind field study area was imaged is denoted by SA. The vertical bar denotes the change in pitch angle (0.024°) necessary to produce a 10 meter per second apparent motion (in an east-west direction) at the subsatellite point over a two-image sequence (24.6 minutes). The changes in pitch angle suggested by the sawtooth portion of the series was not detected in the data images studied; the actual pitch stability was much better than suggested by the sawtooth portions of the data. However, the occurrence of the large pitch dip at 1055 minutes GMT was verified.

in this manner. It is not really expected that the satellite's attitude will change in a discontinuous manner as suggested by the curves, but certainly some smoothed approximation would be expected if the telemetry control system were behaving in such a manner. It appears instead that the yaw and pitch were almost constant in value (apart from the large dip around 1055 minutes GMT) equal to the mean position of each of the sawtooth curves over the ranges investigated.

(2) The large roll and pitch dip occurring at 1055 minutes GMT is definitely reflected in the image data.

(3) The roll telemetry data appears to be accurate to within the rms noise limits. It is possible that with suitable filtering and smoothing that roll pointing accuracies to within a resolution element can be achieved.

(4) An element direction oscillation as a function of scan line was detected in one of the three ATS-6 data images with an amplitude of approximately two elements and a period of 120 mirror scan lines (2.4 minutes). There is no indication in the attitude data that suggests these quasi-sinusoidal oscillations. At present, its source is unexplained; however, a procedure which has had some success has been developed to compensate for them. This is discussed in the next subsection.

ATS-6 Attitude Tests and Results

To examine the reliability and accuracy of the ATS-6 telemetry data, the following was done:

(1) Relative image coordinate displacements of land free from clouds were measured between ATS-6 image data pairs using the same image matching technique discussed above. Sampling was taken over as wide a range as feasible and the components of these satellite image displacement vectors (lines and elements) plotted as a function of mirror scan number. These plots, then, represent the relative coordinate shifts between data image pairs as a function of time.

(2) Relative line and element displacements between image pairs were predicted as a function of time (mirror scan number) with the ATS-6 navigation model using a piece-wise approximation to the telemetry data. (Up to the end of the current contract period, there were too many other sources of error, which had to be dealt with first, to justify a more sophisticated approximation to the attitude telemetry time series).

The results for the image pair 1706z and 1731z (denoted by their start times in hours and minutes) appear in FIGURES III.5 and III.6. Several comments are in order to interpret these figures.

(1) A piece-wise linear approximation to the attitude telemetry data displayed in the previous subsection was used in predicting the relative displacement curves. For FIGURE III.6, the yaw/pitch sawtooth features were incorporated into the model

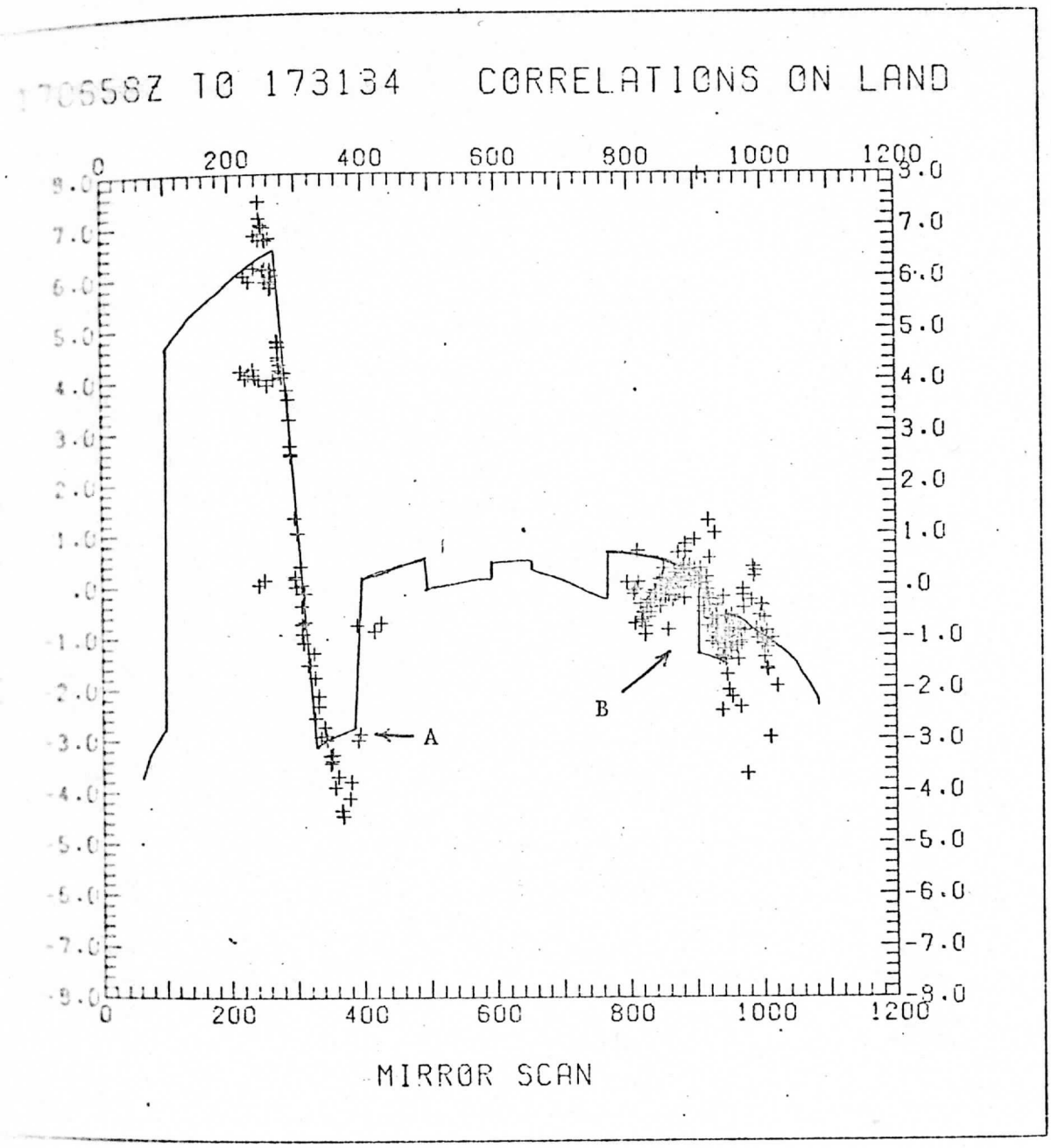

FIGURE III.5. Relative Line Displacements Between Images 1706Z and 1711Z as a Function of Mirror Scan Number. Scattered points are measured values; the solid line is predicted from the ATS-6 model using a piece-wise linear approximation to the roll telemetry data holding yaw and pitch constant. The predicted values were computed at the center of each scan line. (See text for comments referring to areas "A" and "B" in figure.)

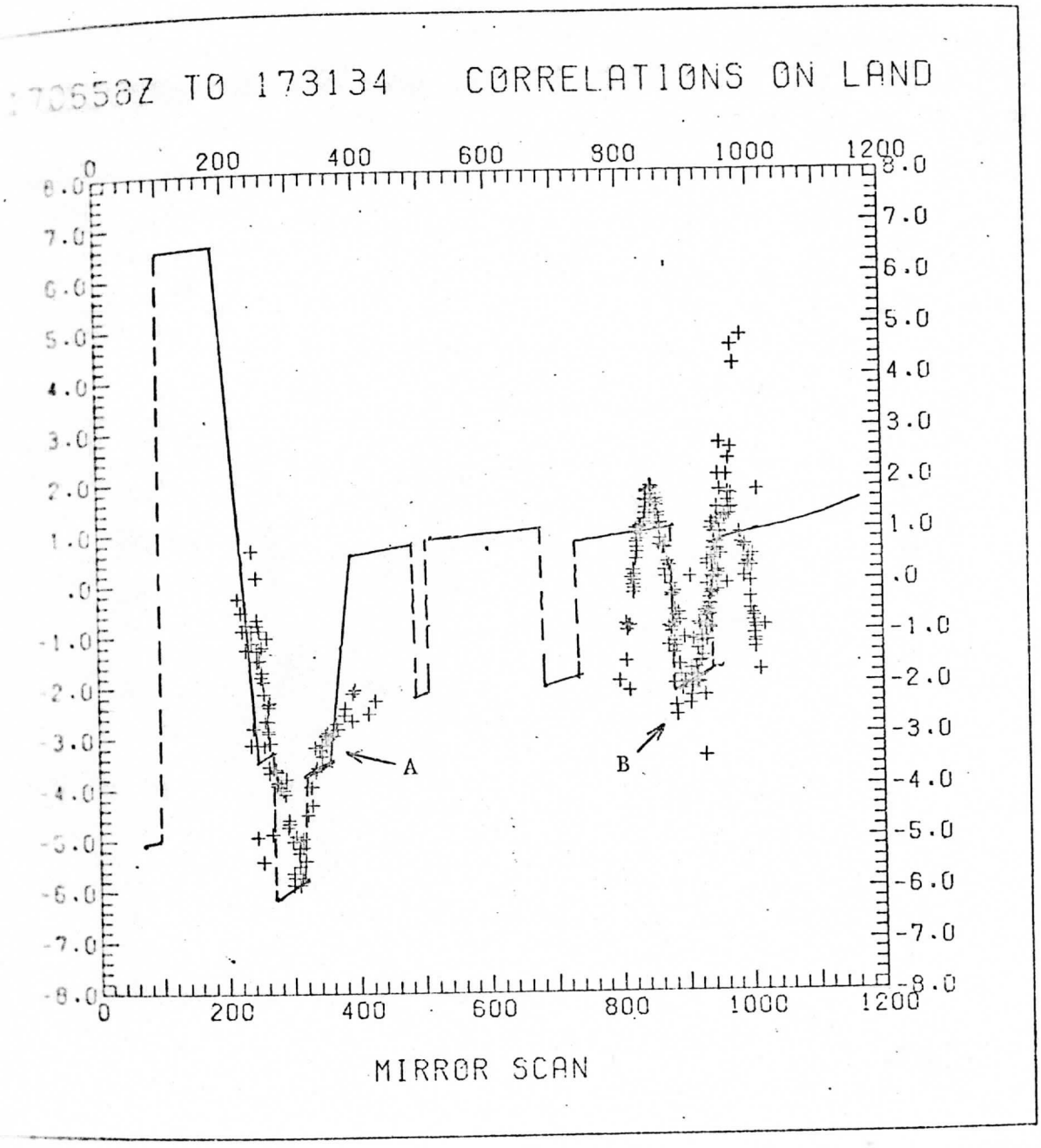

FIGURE III.6. Relative Element Displacements Between Images 1706Z and 1731Z as a Function of Mirror Scan Number. Scattered points are the measured values; the solid line is predicted from the ATS-6 model using a piece-wise linear approximation to the yaw, roll, and pitch attitude telemetry data. The measured oscillations shown above are predominantly from image 1706Z. The cause or source of these oscillations is unknown. (See text for comments referring to areas "A" and "B" in figure.)

which explains the discontinuities. For FIGURE III.5, only the piece-wise linear approximation to the roll was used. Yaw and pitch angles were set equal to constant values which were computed in a round-about manner using landmark measurements. The procedure used is discussed in section IV.

(2) The large dip in the attitude telemetry data at 1055 minutes GMT is verified to be a real change in attitude both in roll and pitch angles. The corresponding mirror scan regions in which the dip occurs is denoted by the letter A in FIGURES III.5 and III.6. Considering that the attitude data were approximated by a piece-wise curve, the agreement between the measured and predicted roll angle effects shown in FIGURE III.5 is quite good.

The agreement between measured and predicted values in FIGURE III.6 is not good not only because the yaw/pitch sawtooth approximations were included in the predicted curve, but also because the quasi-sinusoidal oscillations (predominantly from Image 1706) are making their appearance. The measured oscillations (denoted by B) are quite obvious. The measured data around A is a combination of the pitch attitude dip and the oscillations. This was deduced by measuring image coordinate displacements between image pairs 1642 → 1706 and 1642 → 1731. The 1642 → 1706 plot of these measurements showed a quasi-sinusoidal oscillation with no dip while the 1642 → 1731 plot showed the predicted pitch dip and was free of the oscillations (barring the discontinuous jump). It is worth mentioning that the differences of measured values between image pairs

1642 → 1706 and 1642 → 1731 agreed with the 1706 → 1731 measured values. This result serves to prove the reliability of this image pair-displacement measurement technique.

(3) In FIGURE III.5 it is noted that the general appearance of the predicted "LINE SHIFTS" curve is concave downward. The explanation for this has its basis in the manner in which the attitude control system works (or more accurately, as we perceive it to have worked). For a geosynchronous satellite in an orbit with a nonzero but small inclination angle, i, the subsatellite point oscillates along the same earth meridian about a point centered on the equator with a period of one sidereal day and an amplitude i (earth latitude). Thus, from the point of view of the satellite, the earth is rocking back and forth about an axis perpendicular to the plane formed by the earth's spin axis and a line drawn from the satellite to the earth-center. If the satellite has just passed through the earth's equatorial plane heading southward -- as it had done for the three DAY 195 images discussed in this report -- there will be an apparent northward shift of landmarks between successive images. The shift will be greatest at the subsatellite point and decrease to zero for landmarks near the earth's edge. (There are also second order east/west shifts, but for the purposes of this discussion they can be ignored).

Now the satellite attitude control system tends to roll the satellite about an axis parallel to the earth's

ficticious "rock" axis in such a manner as to keep a landmark located close to the subsatellite point fixed in satellite image coordinates from one image frame scan to the next. This is equivalent to adding a southward pointing vector equal in magnitude to the apparently northward shifted landmarks near the subsatellite point. But in making this roll maneuver, the same southward vector is added to every point in the image. Thus, landmarks near the earth's edge which originally had no shift now have the largest shift -- all southward. Therefore calculated line shifts between two successive images as a function of mirror scan should show approximately zero shift near the earth-center (around mirror scan number 600) and a line shift difference that continues to increase in magnitude for mirror scan values away from 600, the general appearance of which is evident in the predicted curve in FIGURE III.5.

The explanation for the concave nature of this curve also serves to explain the spread in the measured data denoted by B. The predicted curve was computed for landmarks which effectively lie on a meridian passing through the subsatellite points (or more precisely at the center of each sweep line containing the earth image). But the measured data set (B) is a pooled set of measurements obtained by sampling at several element positions along mirror scan lines and therefore contains varying line shift measurements.

(4) Note in FIGURES III.5 and III.6 that the measured line and element shifts tend to be biased towards (lumped around) integer values. This is a result of an inherent weakness in the present image matching techniques. The biasing becomes quite evident whenever near identical images are correlated and is due to the difficulty in interpolating to fractional image coordinates from a very sharp correlation peak derived from quantized digital data. Since this image matching algorithm[†] is the same one used for cloud displacement measurements, the question arose as to its biasing effect on wind measurements. A test was carried out shortly before writing this report but the results were somewhat inconclusive and therefore will have to be repeated at a later date. It was learned, however, that the biasing towards integer values in cloud displacement measurements was not as severe as for land displacement measurements. This is undoubtedly due to the fact that in the latter case near-identical images are being correlated, while in the former case the change in brightness values of a cloud over a two-image 24 minute time period is great enough to smooth out the correlation peaks and therefore allow easier interpolation.

[†]E. A. Smith and D. R. Phillips, "Automated Cloud Tracking Using Precisely Aligned Digital ATS Pictures," IEEE Trans. on Computers, Vol. C-21, pp. 715-729, July 1972.

4. Quasi-Sinusoidal Element Oscillations in the ATS-6 Image Data

In order to determine the presence of the oscillations in Image 1706 over mirror scan ranges for which no cloud-free land appeared in the image data, the image matching technique was used to measure element shifts of the earth edges. Earth edge displacement measurements were also taken over mirror scan regions which overlapped the land displacement measurements (discussed in the previous subsection). There was good agreement between these measurements.

FIGURE III.7 shows a smoothed set of earth edge measurements taken over a mirror scan region which includes both the study area and the equator. Also shown is the predicted element curve based on a piece-wise linear approximation to the pitch telemetry data. For regions around the equator, the effect of any roll or yaw changes on image-pair element shifts would be negligible; thus, it can be argued that shifts measured around this region would be primarily pitch effects and therefore a direct comparison can be made between the measured and predicted curves without concern over other influencing factors. It is apparent from FIGURE III.7 that the pitch telemetry data cannot be used to account for the measured curve.

To account for these oscillations in the wind measurement study the curves for each image pair were approximated by a ninth degree polynomial and used to correct the measured cloud displacement image coordinate element value of the second cloud image displacement relative to the first for each image pair over which cloud displacements were measured. This procedure accounted for most of element oscillation error. Its accuracy is presently limited by the image matching technique which biases the element displacement measurements towards integer values and therefore makes accurate curve fitting difficult.

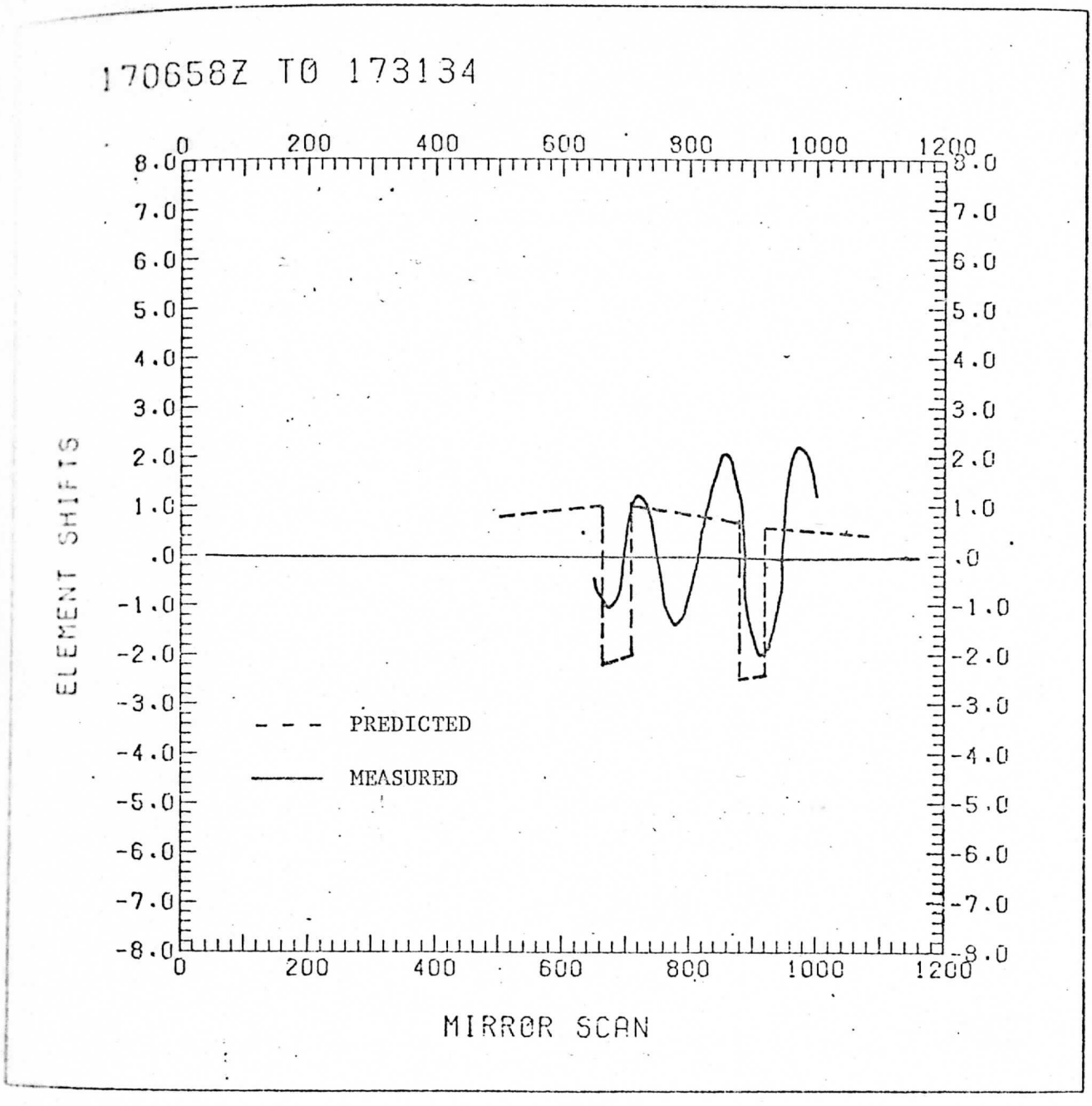

Figure III.7. Relative Element Displacements Between Images 1706Z and 1731Z as a Function of Mirror Scan Number. The predicted curve was derived using a piece-wise linear approximation to the pitch telemetry data for the two images. The measured values derived from the earth edge were smoothed and fit with the curve shown above. These curves span the mirror scan range including the equator and the study area (see text).

IV. DESCRIPTION OF THE MODEL EMPLOYED IN ATS-6 WIND COMPUTATION

This section discusses the key steps involved in computing wind measurements from McIDAS - derived image coordinate displacements. The mathematical details of the general model appear in APPENDIX A.

1. Basic Steps Involved in Wind Computation

For convenience let the three ATS-6 DAY 195 images, 1642, 1706, and 1731 (denoted by their start times) which were used in the ATS/SMS wind comparison study be denoted by T_1, T_2, T_3 respectively.

Let:

(LINI, ELEI) be the location of a cloud measurement in satellite image coordinates (line and element) for image T_I;

(θ_I, ϕ_I), the associated earth coordinates (geodetic latitude and longitude), respectively;

Δt, the time interval between two successive ATS-6 image frame scans for the same cloud feature;

$\bar{R}$, the mean earth radius,

(u_{IJ}, v_{IJ}), the easterly and northerly components of the wind velocity vector of a cloud whose displacement was measured from T_I to T_J.

The basic steps involved in wind computation are as follows:

(1) Using McIDAS, the displacement of a cloud image is measured in satellite image coordinates using the image matching technique discussed in previous sections for $T_1 \rightarrow T_2$ and $T_2 \rightarrow T_3$.

Consider the image coordinates (LIN1, ELE1), (LIN2, ELE2) for $T_1 \rightarrow T_2$ first.

(2) ELE2 is corrected for the quasi-sinusoidal oscillation relative to ELE1 using the curve-fit discussed in the previous section, i.e.

$$\text{ELE2}' \leftarrow \text{ELE2} \; . \tag{1}$$

(3) The satellite image coordinates are transformed to earth coordinates using the ATS-6 model

$$\begin{aligned} (\theta_1, \phi_1) &\leftarrow (\text{LIN1}, \text{ELE1}) \\ (\theta_2, \phi_2) &\leftarrow (\text{LIN2}, \text{ELE2}') \; . \end{aligned} \tag{2}$$

(4) The velocity of the cloud is calculated from the earth coordinates and, Δt, their image time interval

$$\begin{aligned} u_{12} &= \bar{R} \cos((\theta_1 + \theta_2)/2)(\phi_2 - \phi_1)/\Delta t \\ v_{12} &= \bar{R} (\theta_2 - \theta_1)/\Delta t \; . \end{aligned} \tag{3}$$

(5) The procedure is repeated for $T_2 \rightarrow T_3$ for the same cloud, resulting in velocity components u_{23} and v_{23}.

(6) The final velocity of the cloud (u,v) is computed by averaging the velocities from $T_1 \rightarrow T_2$ and $T_2 \rightarrow T_3$

$$\begin{aligned} u &= (u_{12} + u_{23})/2 \\ v &= (v_{12} + v_{23})/2 \; . \end{aligned} \tag{4}$$

From our ATS/SMS wind measurement analysis, it appears that the greatest source of uncertainty in the accuracy of ATS-6 winds enters in step (2), where the image coordinates are transformed to earth coordinates. Specifically, the greatest errors are introduced in transforming from image coordinates using the attitude telemetry data to the associated pointing

vector in the Local Vertical (LV) frame. This key transformation is discussed in the next subsection.

3. Key Transformation Used for Calculating Winds

In order to understand the transformation which has the greatest impact on the accuracy of ATS-6 wind measurements, a few definitions are necessary.

There are three coordinate systems given consideration in this discussion: the Local Vertical (LV), Body-Centered (BC) and Picture Frame (PF). Their origins and axes are nominally conincident and situated at the center of the satellite. The LV +z-axis points from the LV origin to earth center; the LV +x-axis is parallel to the earth's equatorial plane and nominally points east. This coordinate system is independent of the satellite's attitude. The orientation of the BC frame relative to the LV system is defined by the time dependent Euler angles which in part make up the attitude telemetry data. The PF +z-axis points to the center of the image; the PF +x-axis is parallel to the center mirror scan line and nominally points east. The y-axes are inferred from each of the three right-handed orthogonal coordinate systems and nominally point south.

Define:

$\hat{r}_{PF}$ = unit PF pointing vector derived directly from satellite image coordinates (line and element) using the satellite imaging frame geometry,

$\hat{r}_{BC}$ = unit BC pointing vector derived from $\hat{r}_{PF}$,

$\hat{r}_{LV}$ = unit LV pointing vector derived from $\hat{r}_{BC}$,

$\alpha = (\theta_y, \theta_r, \theta_p)$, which in general represent the Euler yaw, roll and pitch angles respectively,

$\bar{\alpha} = (\bar{\theta}_y, \bar{\theta}_r, \bar{\theta}_p)$, Euler angles which define the orientation of the PF relative to the BC system and are generally considered to be time-independent over an interval of several hours,

$\alpha(t) = (\theta_y(t), \theta_r(t), \theta_p(t))$, the Euler angles making up the attitude time series which provide the linkage between the LV and BC coordinate systems,

$\langle\alpha\rangle$ = average value of $\alpha(t) = (\langle\theta_y\rangle, \langle\theta_r\rangle, \langle\theta_p\rangle)$,

R_{PF} = orthogonal rotation matrix which is a function of $\bar{\alpha}$ and transforms $\hat{r}_{BC}$ into $\hat{r}_{PF}$,

R_{BC} = orthogonal rotation matrix which is a function of $\alpha(t)$ (or $\langle\alpha\rangle$) and transforms $\hat{r}_{LV}$ into $\hat{r}_{BC}$,

$S(\alpha) = \sum_{\ell} \| \hat{r}_{PF} - R(\alpha)\, \hat{r}_{LV} \|^2$ = sum over all landmark measurements, ℓ, of the differences between measured satellite image coordinates, $\hat{r}_{PF}$, of each landmark and their associated PF pointing vector, $R(\alpha)\hat{r}_{LV}$, calculated from earth coordinates. In finding an optimal navigation transformation, a value of α is found which minimizes $S(\alpha)$; this value of α is then used in R to transform an arbitrary $\hat{r}_{PF}$ into the LV frame.

From the definitions above,

$$\hat{r}_{PF} = R_{PF}\,(\bar{\alpha})\ \hat{r}_{BC} \tag{1}$$

$$\hat{r}_{BC} = R_{BC}(\alpha(t))\ \hat{r}_{LV}\ . \tag{2}$$

Combining (1) and (2) and solving for $\hat{r}_{LV}$, we have the general transformation from the PF to the LV frame,

$$\hat{r}_{LV}(t) = R^{T}_{BC}(\alpha(t))\ R^{T}_{PF}(\bar{\alpha})\ \hat{r}_{PF} \qquad (3)$$

where, T, is the transpose of the 3 x 3 orthogonal matrices representing the transformations. (Their explicit form is given in APPENDIX A).

Equation (3) is the equation about which most of the efforts of this study have been centered. The problem is to find the best estimate of $\alpha(t)$ in R^{T}_{BC} to minimize the error in transforming $\hat{r}_{PF} \rightarrow \hat{r}_{LV}$. Once $\hat{r}_{LV}$ is correctly computed, the transformation from it to earth coordinates depends only on the orbital equations which introduce additional errors negligible compared to the attitude uncertainties. ($\bar{\alpha}$ is also unknown and must be determined; but this is relatively easy. Errors in $\bar{\alpha}$ will have little effect on the relative navigation of ATS-6 data.)

The values $\alpha(t)$ and $\bar{\alpha}$ actually used in the ATS-6 model were determined as follows:

(1) Assume that the yaw and pitch attitude angles in $\alpha(t)$ are constant; their initial values, $\langle\theta_y\rangle_0$, $\langle\theta_p\rangle_0$ were chosen from the attitude telemetry data plots. The roll angle $\theta_r(t)$ was approximated by a piecewise linear curve.

Minimize $\sum_{\ell} \|\hat{r}_{PF} - R_{PF}(\alpha)\ \hat{r}_{BC}\|^2$ to find $\bar{\alpha}$, and hence $R_{PF}(\bar{\alpha})$, where $\hat{r}_{BC} = R_{BC}(\langle\theta_y\rangle_0, \theta_r(t), \langle\theta_p\rangle_0)\ \hat{r}_{LV}$. (4)

(2) Assume the attitude over an image frame interval is constant, thus $\hat{r}_{PF} = R\ \hat{r}_{LV}$. (5)

This form is equivalent to setting R_{BC} = unit matrix and using for R, the same functional form as for R_{PF}. R is then a

function of 3 Euler angles, the optimum values of which can be found by minimizing

$$\sum_{\ell} |\hat{r}_{PF} - R\,\hat{r}_{LV}|^2 \qquad (6)$$

to get $\bar{R}$.

Now $\bar{R}$ can be considered to be equal to $\bar{R} = \overline{R_{PF}\,R_{BC}} = \overline{R_{PF}}\;\overline{R_{BC}}$ and assuming $R_{PF}(\bar{\alpha}) = \bar{R}_{PF}$, then

$$R_{BC}(\langle\alpha\rangle_1) = \bar{R}_{BC} = R_{PF}^T\,\bar{R}\,, \qquad (7)$$

where $\langle\alpha\rangle_1$ is an improved estimate of $\langle\alpha\rangle_0$.
Since the right hand side of (7) is known explicitly, and the functional form of the left hand side, $R_{BC}(\langle\alpha\rangle_1)$ is known, $\langle\alpha\rangle_1$ can be solved for. The values $\langle\theta_y\rangle_1$ and $\langle\theta_p\rangle_1$ from $\langle\alpha\rangle_1$ were used in the final form of Equation (3), while, the form of $\theta_r(t)$ used in Equation form was retained.

The form of the key transformation used in the ATS-6 navigation model to generate the wind measurements was

$$\hat{r}_{LV}(t) = R_{BC}^T(\langle\theta_y\rangle_1, \theta_r(t), \langle\theta_p\rangle_1)\; R_{PF}^T(\bar{\theta}_y, \bar{\theta}_r, \bar{\theta}_p)\; \hat{r}_{PF}\,, \qquad (8)$$

where,

$\bar{\theta}_y = 1.731°$ $\qquad$ $\langle\theta_y\rangle = -1.0799°(358.920°)$

$\bar{\theta}_r = .379°$ $\qquad$ $\theta_r = \theta_r(t)$

$\bar{\theta}_p = -1.449°$ $\qquad$ $\langle\theta_p\rangle = -1.600°$.

These values were updated by adjusting the imaged field of view angles to minimize landmark residuals and appear in the next section under Subsection 4. These updated values having just recently

been generated have not been used in the ATS-6 model to measure winds. Their only effect would be to improve absolute navigation accuracy - they would not account for the velocity differences observed between ATS-6 and SMS winds.

ERROR ANALYSIS

From our studies, it appears that a major contribution to reducing errors in the ATS-6 wind velocities would be the proper estimation of the roll attitude time series. A secondary source of error results from the quasi-sinusoidal oscillations. Both of these problem areas have solutions in sight. There is also the effect of mirror scan nonlinearities on the accuracy to which image displacements can be measured, but it is felt that this problem is minor. Finally there are problems which affect absolute navigation and are documented in this section for completeness.

1. Effect of Roll Angle Uncertainties on Wind Components

From the roll attitude telemetry plot in FIGURE III.4, it can be seen that the magnitude of quantization and noise has a spread of approximately 0.02 degrees. This subsection shows that, assuming the ATS-6 velocity errors were due to uncertainties in roll angle, that the range of estimated roll errors derived from the v-component velocity measurements falls within the quantization and noise limits of the roll attitude telemetry data. This suggests that the proper filtering and estimating of these data could substantially reduce the v-component error.

Using the definitions and equations from Subsection 1, Section IV, we have from Equation (3) the v-component of the wind velocity derived from the image displacement coordinates between images T_1 and T_2, v_{12}, given as:

$$v_{12} = \overline{R} (\theta_2 - \theta_1)/\Delta t \qquad (1)$$

where $\bar{R}$ is the mean earth radius; θ_1 and θ_2, the initial and final latitude locations of the cloud; and, Δt, the time interval over which the displacement, $(\theta_2 - \theta_1)$, takes place.

For the same cloud we also have the SMS-1 v-component velocity measurement, $\bar{v}_{SMS}$, given as

$$\bar{v}_{SMS} = (v_{12} + v_{23})_{SMS}/2 \tag{2}$$

where $\bar{v}_{SMS}$ is considered to be the correct v-component of the cloud's velocity and

$$\Delta v_{12} = v_{12} - \bar{v}_{SMS} , \tag{3}$$

where Δv_{12} is the error in v_{12}.

Now, as discussed in Subsection 3, Section III, the satellite tends to track the same landmark keeping its satellite image coordinates fixed in successive image frames. To accomplish this for a geosynchronous non-zero inclination orbit, the roll angle must be constantly changing. Thus, a point on the earth with a latitude, θ, imaged at time, t, can be thought of as a smoothly varying function of, θ_r, the nominal roll angle and, β_i, which collectively denotes all the other parameters required to specify the orientation of the mirror (or pointing vector) at time t,

$$\text{i.e.} \quad \theta = \theta(\theta_r, \beta_i), \tag{4}$$

where θ_r and β_i are implicit functions of t. Considering Equation (4) at some instant, t, we can treat the relationship between θ, θ_r, and β_i as purely a geometric relationship and not have to be concerned about the dynamics. Now a small change in θ_r, $\Delta\theta_r$, from its nominal value can be considered to result in an error or change in θ, $\Delta\theta$, which is calculated as

$$\Delta\theta \cong F_1 \, \Delta\theta_r , \tag{5}$$

$$F_1 = \frac{\partial\theta}{\partial\theta_r}\Bigg]_{\theta_{r_1},\, \beta_{i_1},}$$

where θ_{r_1}, β_{i_1} are the nominal values at time t. Equation (5) gives the error in θ as a function of θ_r and $\Delta\theta_r$. The errors resulting from β_i are assumed to be negligible. β_i includes such parameters as yaw and pitch which appear to be nearly constant and in any case would only contribute to second order effects to the v-component errors. Other parameters such as mirror sweep angle can be calculated to a reasonable degree of precision.

The ATS-6 study area is close enough to the subsatellite point and small enough such that the variations in F_1 for different locations contained within it are small compared to the roll quantization and noise. The same value, F_1, therefore can be used for the entire study area. For the subsequent image, we have a value F_2 which can be considered to be equal to F_1 plus a small additive constant due to the slight changes in earth/satellite geometry. This constant when multiplied by the roll error is small enough to be ignored. Thus the value of F_1 can also be used for the second image.

From Equations (1) and (5) we can compute the velocity error, Δv_{12}, and relate it to the roll error

$$\Delta v_{12} \cong \bar{R}/\Delta t \ (\Delta\theta_2 - \Delta\theta_1) \tag{6}$$

$$\Delta v_{12} = \bar{R}/\Delta t \ F_1 (\Delta\theta_{r2} - \Delta\theta_{r1}) \tag{7}$$

Equation (6) relates Equation (7) to the measured error and therefore

$$\Delta\theta_{r_2} - \Delta\theta_{r_1} = F_1 \Delta t/\bar{R} \ (v_{12} - \bar{v}_{SMS}) \tag{8}$$

A similar equation holds for $\Delta\theta_{r_3} - \Delta\theta_{r_2}$ which is derived from $v_{23} - \bar{v}_{SMS}$. The velocity errors appear in columns (2) and (4) in TABLE V.1; their associated roll errors in columns (3) and (5) which were calculated from

(1) Mirror Scan Number	(2) $V_{12} - \bar{V}_{SMS}$ (m/s)	(3) Roll Error Assoc. with Col.(2) ($\times 10^{-3}$ deg)	(4) $V_{23} - \bar{V}_{SMS}$ (m/s)	(5) Roll Error Assoc. with Col.(4) ($\times 10^{-3}$ deg)	(6) Roll Error Sum [Col.(3) + Col.(5)] ($\times 10^{-3}$ deg)
740	-1.29	- 2.7	3.35	7.1	4.4
750	-4.49	- 9.5	4.17	8.8	- 0.7
752	-4.96	-10.5	3.56	7.5	- 3.0
754	-4.29	- 9.1	2.40	5.1	- 4.0
771	-4.28	- 9.1	4.13	8.7	- 0.4
787	-1.92	- 4.1	- .19	0.4	- 3.7
805	-1.74	- 3.7	-4.92	-10.4	-14.1
825	- .12	- 0.3	-3.09	- 6.4	- 6.7

TABLE V.1. Estimated Roll Errors Derived from v-Component Velocity Measurements. Each entry in columns (2) and (4) is the difference between the ATS-6 v-components (v_{ij}) and the SMS averaged v-component ($\bar{V}_{SMS}$) for the same cloud. (v_{ij} is the velocity measured from ATS-6 images T_i and T_j). The assumption is made that $\bar{V}_{SMS}$ is the correct v-component velocity of the cloud and that differences between the ATS-6 and SMS v-components are due to ATS-6 roll uncertainties used in the ATS-6 model. From these velocity differences the resulting roll errors are calculated and displayed in columns (3) and (5).

Equation (8) with

$F_1 = 6.3,$

$\Delta t = (24.6 \text{ min})\ (60 \text{ s/min}),$

$\bar{R} = 6.37 \times 10^6 \text{ m}.$

The calculated roll errors, $\Delta\theta_{r_2} - \Delta\theta_{r_1}$, appearing in column (3) are, of course, the combined roll errors corresponding to the two images T_1 and T_2 for which the ATS-6 v-component v_{12} was measured. There is no way that the individual errors can be calculated using the method above. However, it is apparent that their combined sum is smaller than the quantization and noise present in the roll telemetry data which is on the order of 20×10^{-3} degrees. Therefore, the analysis in this subsection strongly suggests that the errors caused in the ATS-6 v-components could be accounted for by the roll uncertainties, which with proper filtering and curve averaging could be reduced to more acceptable limits.

2. Effect of Quasi-Sinusoidal Oscillations on the Image Data

These oscillations are discussed in detail in Subsection 4, Section III, and as previously mentioned are primarily present in Image 1706. They have no apparent relationship to the attitude telemetry data and conceivably may have been introduced during ground processing. This possibility is presently being investigated.

In the wind measurement analysis they were accounted for by curve fitting the measured earth-edge element displacements between image pairs. The accuracy of the curve is limited by the measurement bias produced by the image matching technique. It appears that the maximum error introduced

in the 3-image average by not having the proper curve is on the order of 2 m/s in the u-components of the velocity vectors.

3. Effect of Mirror Scan Nonlinearities on Wind Components

The background on this problem is given in Subsection 1, Section III. To determine the effect of the mirror scan nonlinearities on the wind components, several small clouds were selected as a test set and their image displacements measured between successive image frames for three different conditions. Each condition consisted of reformatting the data images with the alternate scan lines shifted by the same amount, ΔE, and measuring the displacements, ΔL_{ij}, ΔE_{ij}, of the test clouds in image coordinates, where ΔL_{ij}, ΔE_{ij}, are the line and element displacements. respectively, between the i^{th} and j^{th} images. This was done for $\Delta E = 8,9,10$ where $\Delta E = 8$ and 9 generally resulted in the least distorted cloud images. The results for ΔL_{ij} appear in TABLE V.2. (The ΔE_{ij} measurements are not shown

ΔL_{12} for ΔE =			ΔL_{23} for ΔE =		
8	9	10	8	9	10
- .22	- .20	- .17	.80	1.06	.81
- .14	- .09	- .05	- .05	.04	.11
- .08	- .04	0.00	.17	.47	.22
- .86	- .92	- .71	.25	.48	.25
- .55	- .85	- .78	.79	.91	.45
.07	.05	.06	1.23	1.44	1.40
- .91	- .93	- .73	.69	.75	.45
-1.82	-2.17	-2.28	- .18	- .25	- .16
- .83	-1.23	- .86	- .09	- .17	- .12

TABLE V.2. Effect of Mirror Scan Nonlinearities on Line Measurements. Values in table are line displacements calculated by the image matching technique discussed above between images T_i and T_j of the comparison test clouds discussed in Section II for images whose alternate mirror scan lines were displaced relative to each other by an element difference, ΔE, equal to 8, 9 and 10 elements.

cause their differences for different ΔE were substantially smaller). ere, each of the row values corresponds to measured displacements in line rection for the same test cloud. Changes in the line direction redominantly affect the v-components of the wind velocity vectors. If iere is any significant difference among any of the columns for each of ie ΔL_{ij}, it is in the middle column $\Delta E = 9$ for ΔL_{23}. A t-test made on the ifferences of each of the columns taken in pairs for fixed ΔL_{ij} supported iis impression. (The middle column was significantly different from the ther two on the .05 level). The other columns were not significantly fferent from each other.

In any case, the differences between ΔL_{12} and ΔL_{23} for the same loud tend to be much larger that the differences due to changes in ΔE r each ΔL_{ij}. Since the differences between the ΔL_{ij} are due primarily roll uncertainties (see Subsection 1 in this section), the analysis in iis section indicates that the errors introduced due to relative mirror an nonlinearities are small compared to those introduced by roll angle ncertainties.

A Possible Satellite Image Frame Geometry Problem

There still remains to be solved a small problem affecting the solute navigation accuracy in the ATS-6 data. This subsection documents ie problem and discusses some of the investigations made concerning it.

TABLES V.3 through V.8 are 39 landmark measurements and residuals lculated from the ATS-6 model under different conditions. The first ree tables are landmark measurements for each of the three DAY-195 images ose residuals were calculated assuming a constant attitude for the duration

```
INPUT DAY.
INPUT ORBIT
ENTER 1 FOR NAVIGATION---2 FOR RESIDUALS--3 FOR              IDEAL LANDMARKS
ENTER NUM LANDMARKS
ENTER LANDMARKS--TIME,LINE,ELE,LAT,LON
CONVERGENCE AT ITERATION     18
FINAL POINT(DEG):
        YAW          ROLL         PITCH
     .7045334     .3042127     .1590844
GRADIENT NORM= .10343455-14              FINAL VALUE: .30920820-05

ENTER CONTROL  -1=STOP,1=NEW LNDMRKS(IE NEW NAVIGATION),2=RESIDUALS
ENTER NUM LANDMARKS
ENTER LANDMARKS--TIME,LINE,ELE,LAT,LON
```

RESIDUALS

	LANDMARK MEASUREMENTS					RESIDUALS (MEAS-CALC)	
		LIN	ELE	LAT	LON	LIN	ELE
A	164222	391	1346	470000	-844500	-.17	-1.81
	164222	395	1344	464500	-850000	.93	-1.18
	164222	408	1324	453800	-864000	.72	-1.26
	164222	414	1341	451100	-853600	1.05	-.36
	164222	414	1335	450700	-860100	.28	-.68
	164222	420	1333	444200	-861500	1.12	-.46
B	164222	393	1262	465700	-905100	1.66	-2.81
	164222	396	1247	464000	-920000	1.25	-2.27
C	164222	392	1650	475400	-592500	-2.89	1.37
	164222	402	1647	470000	-602600	-2.49	.69
	164222	416	1641	455000	-615800	-1.16	1.06
	164222	423	1656	451800	-610300	-1.51	1.28
	164222	499	1525	385700	-745500	-.66	4.92
E	164222	656	883	293400	-1133200	1.33	-.36
	164222	664	888	290300	-1130900	.76	-.03
	164222	666	882	285700	-1132500	.83	-1.19
	164222	669	897	284300	-1123600	.42	.76
	164222	692	859	272600	-1143000	-.47	-.70
F	164222	682	924	275500	-1105400	.71	.97
	164222	695	901	271300	-1120600	.53	.84
	164222	716	915	260000	-1110700	.52	1.08
	164222	722	915	254000	-1110200	.57	.50
	164222	733	921	250000	-1103800	-.25	1.08
	164222	743	925	242800	-1102100	.18	1.30
	164222	745	897	242500	-1115000	.26	.05
G	164222	790	1630	213000	-725600	-2.45	1.63
	164222	805	1582	204200	-754700	-1.74	1.67
	164222	815	1612	201400	-740900	-1.06	.90
	164222	817	1611	200400	-741700	-2.21	1.76
	164222	844	1639	184300	-725000	-1.54	-.33
	164222	857	1715	180800	-683500	-1.16	-.16
I	164222	1543	1710	-151800	-694600	.13	-1.87
	164222	1557	1714	-160000	-692700	.45	-1.65
	164222	1557	1719	-160000	-691100	.62	-1.28
	164222	1559	1723	-160500	-685300	1.18	-2.24
	164222	1561	1720	-161500	-690530	-.25	-1.21
	164222	1565	1723	-162700	-685600	-.09	-.41
J	164222	1883	1790	-343600	-583000	3.13	.21
	164222	1906	1798	-361900	-564600	1.56	.16

TABLE V.3. DAY 195 Landmark Measurements and Residuals.

Image 1642, Constant Attitude Assumed.

```
ENTER CONTROL  -1=STOP,1=NEW LNDMRKS(IE NEW NAVIGATION),2=RESIDUALS
ENTER NUM LANDMARKS
ENTER LANDMARKS--TIME,LINE,ELE,LAT,LON
CONVERGENCE AT ITERATION      7
FINAL POINT(DEG):
        YAW          ROLL         PITCH
    .7083034     .3359041     .1582899
GRADIENT NORM= .37157419-18          FINAL VALUE: .33700101-05

ENTER CONTROL  -1=STOP,1=NEW LNDMRKS(IE NEW NAVIGATION),2=RESIDUALS
ENTER NUM LANDMARKS
ENTER LANDMARKS--TIME,LINE,ELE,LAT,LON
```

RESIDUALS

		LANDMARK MEASUREMENTS				RESIDUALS (MEAS-CALC)	
		LIN	ELE	LAT	LON	LIN	ELE
	170657	393	1348	470000	-844500	.03	.40
	170657	396	1344	464500	-850000	.14	-.96
A	170657	410	1324	453800	-864000	1.01	-1.06
	170657	415	1341	451100	-853600	.37	-.14
	170657	416	1334	450700	-860100	.60	-1.47
	170657	422	1333	444200	-861500	1.47	-.25
B	170657	394	1263	465700	-905100	.89	-1.63
	170657	397	1248	464000	-920000	.50	-1.10
	170657	395	1650	475400	-592500	-2.13	1.71
C	170657	404	1648	470000	-602600	-2.67	2.04
	170657	418	1641	455000	-615800	-1.25	1.39
	170657	425	1655	451800	-610300	-1.59	.62
	170657	500	1523	385700	-745500	-1.12	3.19
	170657	657	883	293400	-1133200	1.30	-.32
	170657	665	888	290300	-1130900	.76	.02
E	170657	667	881	285700	-1132500	.83	-2.15
	170657	670	896	284300	-1123600	.45	-.19
	170657	693	857	272600	-1143000	-.43	-2.66
	170657	683	922	275500	-1105400	.81	-.97
	170657	696	899	271300	-1120600	.63	-1.10
	170657	717	913	260000	-1110700	.69	-.86
F	170657	722	913	254000	-1110200	-.24	-1.44
	170657	734	919	250000	-1103800	-.03	-.85
	170657	744	923	242800	-1102100	.43	-.63
	170657	746	896	242500	-1115000	.48	-.89
	170657	791	1630	213000	-725600	-2.19	1.86
	170657	806	1583	204200	-754700	-1.39	2.89
G	170657	816	1614	201400	-740900	-.73	3.12
	170657	818	1612	200400	-741700	-1.86	2.98
	170657	845	1641	184300	-725000	-1.19	1.89
	170657	857	1716	180800	-683500	-1.91	1.07
	170657	1543	1712	-151800	-694600	-.48	.14
	170657	1558	1716	-160000	-692700	.81	.35
I	170657	1558	1721	-160000	-691100	.98	.73
	170657	1559	1725	-160500	-685300	.53	-.24
	170657	1562	1721	-161500	-690530	.09	-.21
	170657	1566	1724	-162700	-685600	.25	.59
J	170657	1884	1787	-343600	-583000	2.52	-2.93
	170657	1909	1795	-361900	-564600	2.82	-2.99

TABLE V.4. DAY 195 Landmark Measurements and Residuals.

Image 1706, Constant Attitude Assumed.

```
ENTER CONTROL  -1=STOP,1=NEW LNDMRKS(IE NEW NAVIGATION),2=RESIDUALS
ENTER NUM LANDMARKS
ENTER LANDMARKS--TIME,LINE,ELE,LAT,LON
CONVERGENCE AT ITERATION      6
FINAL POINT(DEG):
       YAW          ROLL         PITCH
    .6548795     .3537243     .1548226
GRADIENT NORM= .27928324-18              FINAL VALUE: .41308430-05

ENTER CONTROL  -1=STOP,1=NEW LNDMRKS(IE NEW NAVIGATION),2=RESIDUALS
ENTER NUM LANDMARKS
ENTER LANDMARKS--TIME,LINE,ELE,LAT,LON
```

RESIDUALS

	LANDMARK MEASUREMENTS					RESIDUALS (MEAS-CALC)	
		LIN	ELE	LAT	LON	LIN	ELE
	173133	393	1348	470000	-844500	-.29	.09
A	173133	397	1345	464500	-850000	.84	-.27
	173133	410	1325	453800	-864000	.80	-.36
	173133	415	1342	451100	-853600	.16	.56
	173133	416	1336	450700	-860100	.41	.23
	173133	421	1334	444200	-861500	.30	.46
B	173133	394	1264	465700	-905100	.69	-.97
	173133	397	1249	464000	-920000	.32	-.45
	173133	396	1649	475400	-592500	-2.19	.52
C	173133	406	1647	470000	-602600	-1.66	.86
	173133	418	1642	455000	-615800	-2.14	2.22
	173133	426	1657	451800	-610300	-1.49	2.45
	173133	501	1523	385700	-745500	-.29	3.04
	173133	657	883	293400	-1133200	2.20	-.53
	173133	665	888	290300	-1130900	1.69	-.18
E	173133	667	882	285700	-1132500	1.76	-1.35
	173133	670	896	284300	-1123600	1.39	-.38
	173133	693	859	272600	-1143000	.57	-.83
	173133	683	924	275500	-1105400	1.79	.86
	173133	696	901	271300	-1120600	1.64	.74
F	173133	717	915	260000	-1110700	1.76	1.01
	173133	723	915	254000	-1110200	1.84	.43
	173133	735	920	250000	-1103800	2.08	.03
	173133	744	924	242800	-1102100	1.57	.27
	173133	746	897	242500	-1115000	1.62	.00
	173133	791	1629	213000	-725600	-1.75	.97
	173133	805	1581	204200	-754700	-1.81	.99
G	173133	815	1612	201400	-740900	-1.20	1.24
	173133	817	1610	200400	-741700	-2.33	1.10
	173133	844	1641	184300	-725000	-1.67	2.03
	173133	857	1715	180800	-683500	-1.57	.24
	173133	1543	1710	-151800	-694600	.03	-1.22
	173133	1557	1713	-160000	-692700	.29	-2.00
I	173133	1557	1719	-160000	-691100	.45	-.63
	173133	1559	1724	-160500	-685300	.97	-.60
	173133	1563	1719	-161500	-690530	1.55	-1.56
	173133	1566	1722	-162700	-685600	.69	-.76
J	173133	1878	1784	-343600	-583000	-4.02	-5.09
	173133	1902	1794	-361900	-564600	-4.85	-3.13

TABLE V.5. DAY 195 Landmark Measurements and Residuals.

Image 1731, Constant Attitude Assumed.

```
ENTER CONTROL  -1=STOP,1=NEW LNDMRKS(IE NEW NAVIGATION),2=RESIDUALS
ENTER NUM LANDMARKS
ENTER LANDMARKS--TIME,LINE,ELE,LAT,LON
CONVERGENCE AT ITERATION      7
FINAL POINT(DEG):
      YAW          ROLL         PITCH
 1.7448271     .3934799 -1.4406357
GRADIENT NORM= .17873834-17              FINAL VALUE: .40996267-05

ENTER CONTROL  -1=STOP,1=NEW LNDMRKS(IE NEW NAVIGATION),2=RESIDUALS
ENTER NUM LANDMARKS
ENTER LANDMARKS--TIME,LINE,ELE,LAT,LON
```

RESIDUALS

	LANDMARK MEASUREMENTS					RESIDUALS (MEAS-CALC)	
		LIN	ELE	LAT	LON	LIN	ELE
	164222	391	1346	470000	-844500	-.72	-2.05
	164222	395	1344	464500	-850000	.38	-1.41
A	164222	408	1324	453800	-864000	.21	-1.49
	164222	414	1341	451100	-853600	.55	-.58
	164222	414	1335	450700	-860100	-.21	-.90
	164222	420	1333	444200	-861500	.64	-.68
B	164222	393	1262	465700	-905100	1.15	-3.04
	164222	396	1247	464000	-920000	.75	-2.51
	164222	392	1650	475400	-592500	-3.59	1.14
C	164222	402	1647	470000	-602600	-3.18	.47
	164222	416	1641	455000	-615800	-1.81	.84
	164222	423	1656	451800	-610300	-2.15	1.06
	164222	499	1525	385700	-745500	-.44	4.77
	164222	656	883	293400	-1133200	.99	-.47
	164222	664	888	290300	-1130900	.44	-.12
E	164222	666	882	285700	-1132500	.51	-1.29
	164222	669	897	284300	-1123600	.11	.67
	164222	692	859	272600	-1143000	-.70	-.78
	164222	682	924	275500	-1105400	.42	.88
	164222	695	901	271300	-1120600	.29	.77
	164222	716	915	260000	-1110700	.33	1.01
F	164222	722	915	254000	-1110200	.40	.43
	164222	733	921	250000	-1103800	-.40	1.03
	164222	743	925	242800	-1102100	.07	1.25
	164222	745	897	242500	-1115000	.17	.00
	164222	790	1630	213000	-725600	-2.80	1.61
	164222	805	1582	204200	-754700	-2.02	1.66
G	164222	815	1612	201400	-740900	-1.33	.89
	164222	817	1611	200400	-741700	-2.47	1.75
	164222	844	1639	184300	-725000	-1.74	-.32
	164222	857	1715	180800	-683500	-1.37	-.14
	164222	1543	1710	-151800	-694600	1.22	-1.46
	164222	1557	1714	-160000	-692700	1.57	-1.23
I	164222	1557	1719	-160000	-691100	1.75	-.86
	164222	1559	1723	-160500	-685300	2.30	-1.82
	164222	1561	1720	-161500	-690530	.88	-.79
	164222	1565	1723	-162700	-685600	1.05	.02
J	164222	1883	1790	-343600	-583000	5.17	.83
	164222	1906	1798	-361900	-564600	3.66	.80

TABLE V.6. DAY 195 Landmark Measurements and Residuals.

Image 1642, Roll Attitude Telemetry Data Used.

ENTER CONTROL -1=STOP,1=NEW LNDMRKS(IE NEW NAVIGATION),2=RESIDUALS
ENTER NUM LANDMARKS
ENTER LANDMARKS--TIME,LINE,ELE,LAT,LON
CONVERGENCE AT ITERATION 6
FINAL POINT(DEG):

YAW	ROLL	PITCH
1.7471070	.3942592	-1.4424828

GRADIENT NORM= .15312701-17 FINAL VALUE: .41428227-05

ENTER CONTROL -1=STOP,1=NEW LNDMRKS(IE NEW NAVIGATION),2=RESIDUALS
ENTER NUM LANDMARKS
ENTER LANDMARKS--TIME,LINE,ELE,LAT,LON

RESIDUALS

	LANDMARK MEASUREMENTS					RESIDUALS (MEAS-CALC)	
		LIN	ELE	LAT	LON	LIN	ELE
	170657	393	1348	470000	-844500	-.33	.16
A	170657	396	1344	464500	-850000	-.22	-1.20
	170657	410	1324	453800	-864000	.69	-1.29
	170657	415	1341	451100	-853600	.05	-.37
	170657	416	1334	450700	-860100	.29	-1.70
B	170657	422	1333	444200	-861500	1.16	-.48
	170657	394	1263	465700	-905100	.57	-1.87
	170657	397	1248	464000	-920000	.19	-1.34
	170657	395	1650	475400	-592500	-2.66	1.48
C	170657	404	1648	470000	-602600	-3.18	1.81
	170657	418	1641	455000	-615800	-1.72	1.17
	170657	425	1655	451800	-610300	-2.05	.40
	170657	500	1523	385700	-745500	-.63	3.04
	170657	657	883	293400	-1133200	.90	-.43
E	170657	665	888	290300	-1130900	.37	-.08
	170657	667	881	285700	-1132500	.45	-2.25
	170657	670	896	284300	-1123600	.06	-.29
	170657	693	857	272600	-1143000	-.73	-2.75
	170657	683	922	275500	-1105400	.44	-1.07
	170657	696	899	271300	-1120600	.31	-1.19
F	170657	717	913	260000	-1110700	.41	-.93
	170657	722	913	254000	-1110200	-.51	-1.51
	170657	734	919	250000	-1103800	-.28	-.92
	170657	744	923	242800	-1102100	.21	-.69
	170657	746	896	242500	-1115000	.28	-.94
	170657	791	1630	213000	-725600	-2.69	1.84
G	170657	806	1583	204200	-754700	-1.83	2.88
	170657	816	1614	201400	-740900	-1.16	3.11
	170657	818	1612	200400	-741700	-2.29	2.97
	170657	845	1641	184300	-725000	-1.57	1.90
	170657	857	1716	180800	-683500	-1.39	1.11
	170657	1543	1712	-151800	-694600	.63	.57
	170657	1558	1716	-160000	-692700	1.95	.79
I	170657	1558	1721	-160000	-691100	2.12	1.17
	170657	1559	1725	-160500	-685300	1.66	.20
	170657	1562	1721	-161500	-690530	1.24	.23
	170657	1566	1724	-162700	-685600	1.40	1.06
J	170657	1884	1787	-343600	-583000	3.85	-2.30
	170657	1909	1795	-361900	-564600	4.20	-2.34

TABLE V.7. DAY 195 Landmark Measurements and Residuals.

Image 1706, Roll Attitude Telemetry Data Used.

```
ENTER CONTROL  -1=STOP,1=NEW LNDMRKS(IE NEW NAVIGATION),2=RESIDUALS
ENTER NUM LANDMARKS
ENTER LANDMARKS--TIME,LINE,ELE,LAT,LON
CONVERGENCE AT ITERATION      6
FINAL POINT(DEG):
        YAW           ROLL          PITCH
  1.6833787     .3888441 -1.4472735
GRADIENT NORM= .19923733-17              FINAL VALUE: .37023056-05

ENTER CONTROL  -1=STOP,1=NEW LNDMRKS(IE NEW NAVIGATION),2=RESIDUALS
ENTER NUM LANDMARKS
ENTER LANDMARKS--TIME,LINE,ELE,LAT,LON
```

RESIDUALS

	LANDMARK MEASUREMENTS					RESIDUALS (MEAS-CALC)	
		LIN	ELE	LAT	LON	LIN	ELE
	173133	393	1348	470000	-844500	-.98	-.23
A	173133	397	1345	464500	-850000	.16	-.60
	173133	410	1325	453800	-864000	.15	-.68
	173133	415	1342	451100	-853600	-.50	.25
	173133	416	1336	450700	-860100	-.24	-.08
B	173133	421	1334	444200	-861500	-.35	.15
	173133	394	1264	465700	-905100	.05	-1.30
	173133	397	1249	464000	-920000	-.29	-.77
C	173133	396	1649	475400	-592500	-3.10	.20
	173133	406	1647	470000	-602600	-2.55	.54
	173133	418	1642	455000	-615800	-3.01	1.92
	173133	426	1657	451800	-610300	-2.36	2.15
	173133	501	1523	385700	-745500	-1.27	2.79
	173133	657	883	293400	-1133200	1.90	-.67
E	173133	665	888	290300	-1130900	1.39	-.31
	173133	667	882	285700	-1132500	1.47	-1.48
	173133	670	896	284300	-1123600	1.09	-.51
	173133	693	859	272600	-1143000	.33	-.95
	173133	683	924	275500	-1105400	1.49	.74
	173133	696	901	271300	-1120600	1.38	.63
F	173133	717	915	260000	-1110700	1.52	.91
	173133	723	915	254000	-1110200	1.60	.34
	173133	735	920	250000	-1103800	1.85	-.05
	173133	744	924	242800	-1102100	1.35	.19
	173133	746	897	242500	-1115000	1.42	-.07
	173133	791	1629	213000	-725600	-2.41	.93
	173133	805	1581	204200	-754700	-2.42	.97
G	173133	815	1612	201400	-740900	-1.82	1.22
	173133	817	1610	200400	-741700	-2.94	1.08
	173133	844	1641	184300	-725000	-2.27	2.04
	173133	857	1715	180800	-683500	-2.20	.25
	173133	1543	1710	-151800	-694600	.32	-.69
	173133	1557	1713	-160000	-692700	.60	-1.46
I	173133	1557	1719	-160000	-691100	.75	-.09
	173133	1559	1724	-160500	-685300	1.28	-.05
	173133	1563	1719	-161500	-690530	1.86	-1.01
	173133	1566	1722	-162700	-685600	1.01	-.21
J	173133	1878	1784	-343600	-583000	3.34	-4.04
	173133	1902	1794	-361900	-564600	2.54	-2.07

TABLE V.8. DAY 195 Landmark Measurements and Residuals.

Image 1731, Roll Attitude Telemetry Data Used.

of each image frame scan interval; the second set of three tables (V.6 to V.8) are again landmark measurements for the three images, only in this case the residuals were calculated using the attitude telemetry data. (Referring to Subsection 2, Section IV, the first condition involved minimizing Equation (6); the second condition, minimizing Equation (4). The calculated satellite coordinates were obtained by using Equation (8) for the second condition). The first two columns in each table are the landmark measurements in satellite coordinates (line and element), the next two columns the associated earth coordinates (latitude and longitude), and the last two columns the resulting residuals (measured minus predicted satellite coordinates). Landmark classes (landmark measurements from approximately the same local area of the image data) are delineated by capital letters.

The striking thing to notice is that for all six tables the line residuals for landmark classes C and G are always large and negative. It is highly unlikely that these features can be explained away as an attitude problem since the same pattern persists over all the images with or without the attitude telemetry incorporated into the model. (Landmark classes I and J are not included in the above discussion since for Image 1731, they were scanned around 1055 GMT when there was a large change in the attitude angles (FIGURES III.4 and III.5)).

It was thought that perhaps the cause of this problem was due to differences between the actual scan field-of-view angles and the nominal values (20 degrees $\times$ 20 degrees). Hence the angle values used in the model were varied in small increments and the residuals computed. The pattern of large negative line residuals for classes C and G was essentially unaffected;

the only effect of changing the field-of-view angles was to reduce the sum of squares of the residuals by a small amount. The angles which resulted in the smallest sums of squares (19.92 degrees step angle, 20.07 degrees sweep angle) were retained in the model and, in fact, were those values used in the calculation of residuals for TABLES V.3 through V.8.

The model itself was thoroughly examined for errors which might account for the pattern observed in the line residuals, but none was found. It is conjectured that the problem might be related to the step-scan mirror geometry.

TABLE V.9 provides a summary of the optimized angles from TABLES V.3 through V.8 under conditions (A) and (B), and in addition, for two other conditions ((C) and (D)) which appear without their associated landmark measurement residual tables. In the terminology of Subsection 2, Section IV, the angles calculated for each of the three images under conditions (B) and (D) refer to $\bar{\alpha}$, the Euler angles defining the orientation of the PF relative to the BC coordinate system. Note for condition (D), derived from the landmark classes A through G, the variation in roll and pitch values for each of the three images in no more than .001 degrees and about .03 degrees for the yaw.

When all landmarks are included (condition (B)), the overall average of each of these angles changes. (The roll angle for T_3 is affected more than the others; it includes the landmarks associated with the 1055 GMT dip which is not accounted for by the roll telemetry data for condition (B)). The additional landmarks which were added to make up the "All Landmarks" category, are landmark classes I and J which are widely separated in scan times (and location) from the others. Including them in the navigation amplifies the line residual pattern discussed above. Note also in the last

CONDITION	IMAGE	YAW (deg)	ROLL (deg)	PITCH (deg)	FINAL VALUE $\times 10^5$
(A)					
Constant Attitude (All Landmarks)	T_1	.706	.304	.159	.309
	T_2	.708	.336	.158	.337
	T_3	.655	.354	.155	.413
(B)					
Roll Telemetry (All Landmarks)	T_1	1.745	.393	-1.441	.410
	T_2	1.747	.394	-1.442	.414
	T_3	1.683	.389	-1.447	.370
(C)					
Constant Attitude (Landmarks A-G)	T_1	.864	.303	.176	.175
	T_2	.852	.335	.173	.204
	T_3	.856	.356	.178	.105
(D)					
Roll Telemetry (Landmarks A-G)	T_1	1.921	.395	-1.423	.173
	T_2	1.896	.395	-1.423	.208
	T_3	1.923	.394	-1.422	.102

TABLE V.9. Summary of Optimized Navigation Angles from Tables V.3 through V.8. Angles for constant attitude conditions (A) and (C) are for the optimized transformation from the Local Vertical Frame to the Picture Frame; angles for conditions (B) and (D) using the roll telemetry data are for the optimized transformation from the Body Centered Frame to the Picture Frame. (T_1, T_2, T_3 refer to the three image frames with start times 1642, 1706 and 1734).

column that the "FINAL VALUE"s (minimum sums of squares of the residuals) increase substantially relative to the values for condition (D). This increase is larger than to be expected if everything were behaving properly since in going from "Landmark A-G" to "All Landmarks," the number of landmark measurements is only increased from 31 to 39. It seems reasonably clear that the problem discussed in this subsection affecting the absolute navigation is a geometrical one; collaboration with the appropriate Goddard personnel hopefully will clear it up.

APPENDIX A

BASIC NAVIGATION MODEL APPLIED TO ATS-6 IMAGE DATA BASE

Contents

NOMENCLATURE

Coordinate Systems (C.S.)

EI = Earth-centered Inertial

ER = Earth-centered Rotating

LV = Local Vertical (satellite-centered)

BC = Body Centered (satellite-centered)

PF = Picture Frame (satellite-centered)

Orthogonal Matrices

R_{LV} = rotation into LV C.S.

R_{BC} = rotation into BC C.S.

R_{PF} = rotation in PF C.S.

R_A = optimized "navigation" matrix

$R(\theta,k)$ = rotation about axis k (k-1,2,3) in a ccw sense by an angle θ

Vectors

$\hat{r}$ = unit vector

$\vec{r}_s$ = satellite radius vector

$\vec{r}_1$ = landmark pointing vector

$\vec{r}_2$ = earth-coordinate, EI C.S.

$\vec{r}_E$ = earth-coordinate, ER C.S.

$\hat{r}_{LV}$ = pointing vector in LV C.S.

$\hat{r}_{BC}$ = pointing vector in BC C.S.

$\hat{r}_{PF}$ = pointing vector in PF C.S.

$\hat{e}_3 = (0,0,1)^T$

Other

$\theta_y, \theta_r, \theta_p$ = attitude yaw, roll, pitch angles

θ_L, ϕ_L = geodetic latitude, longitude

θ_E = sidereal time of Greenwich prime meridian

ρ_L, ρ_E = radians/line, radians/element

λ = mirror step angle

δ = mirror sweep angle

α_i = navigation parameter

$\bar{\alpha}_i$ = optimized navigation parameter

LIN,ELE = satellite image coordinates: Line, Element

L_c, E_c = picture-center coordinates (line, element)

e = eccentricity of earth oblate spheriod model

r_{eq} = earth's equatorial radius

r_p = earth's polar radius

s = distance from satellite to landmark

t = time

t_M = epoch time, lies within image frame interval

$\|\cdot\|$ = Euclidean norm

$|\cdot|$ = absolute value operator

I. PRELIMINARIES

A. Coordinate Systems

All coordinate systems used in the model are 3-D right-handed orthogonal coordinate systems. There are five all together. Two have their origins placed at the dynamical center of the earth.

The plane formed by the x- and y-axes of the earth-centered inertial coordinate system (EI) lies in the earth's equatorial plane. The x-axis points at the vernal equinox (γ) which is assumed to be inertially fixed and the z-axis points north. Rotating relative to this inertial frame is the earth-centered rotating coordinate system (ER) with its x-axis passing through the Greenwich meridian and its z-axis coincident with the EI z-axis (Figure 1).

In the local vertical (LV) system, the z-axis points to the center of the earth, i.e. the unit vector representing this axis at time t is given as $\hat{z} = -\vec{r}_s(t)/\|\vec{r}_s(t)\|$, where $\vec{r}_s$ is the satellite radius vector (Figure 1). The x-axis is parallel to the earth's equatorial plane and nominally points east.

Fixed in the satellite body is the body-centered (BC) coordinate system whose axes are nominally coincident with the LV system. Departures from this alignment are measured by the yaw, pitch, and roll time dependent angles which in part make up the attitude telemetry data. These rotations are explicitly defined later on. Also nominally coincident with these coordinates systems is the last to be defined, the image or picture frame (PF) coordinate system (Figure 2). The z-axis points to the picture center (earth image center) which for ATS-6, is the image point occurring at the midpoint of the mirror sweep angle for the mid-mirror scan number of a full

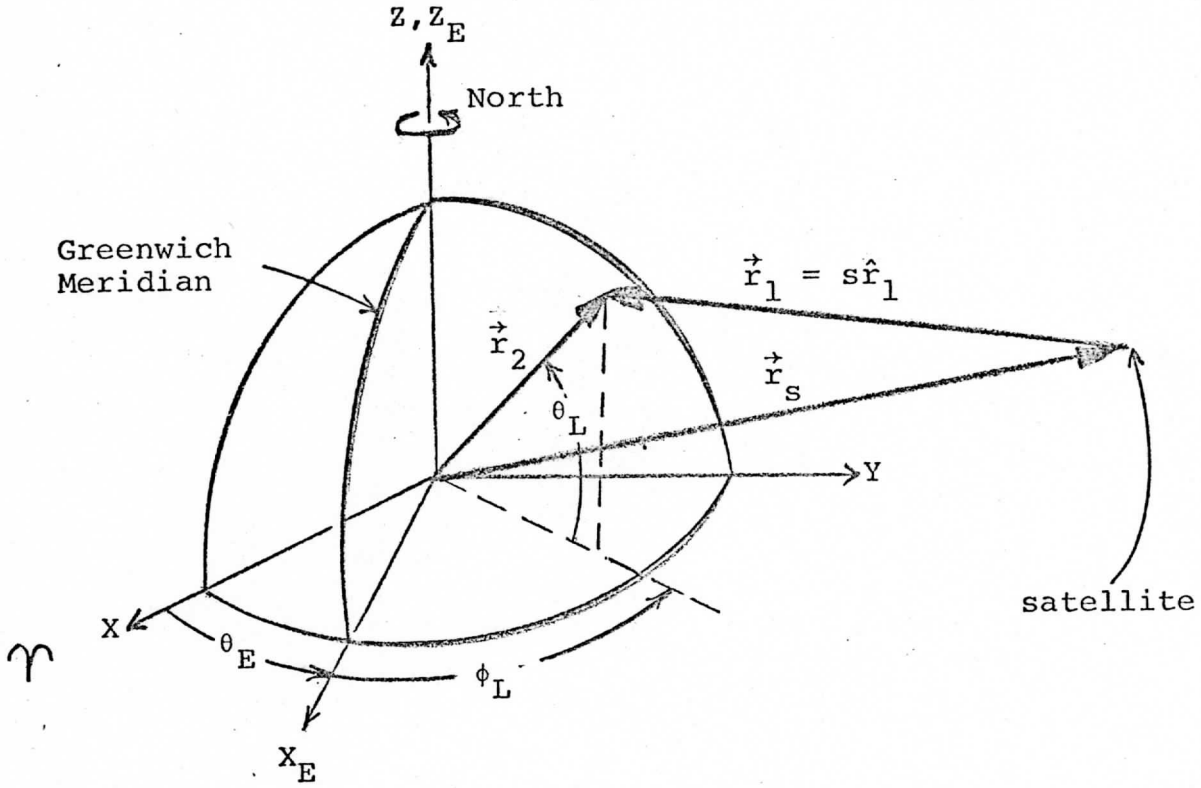

Figure 1. Satellite-Earth Geometry (See Text for definition of symbols)

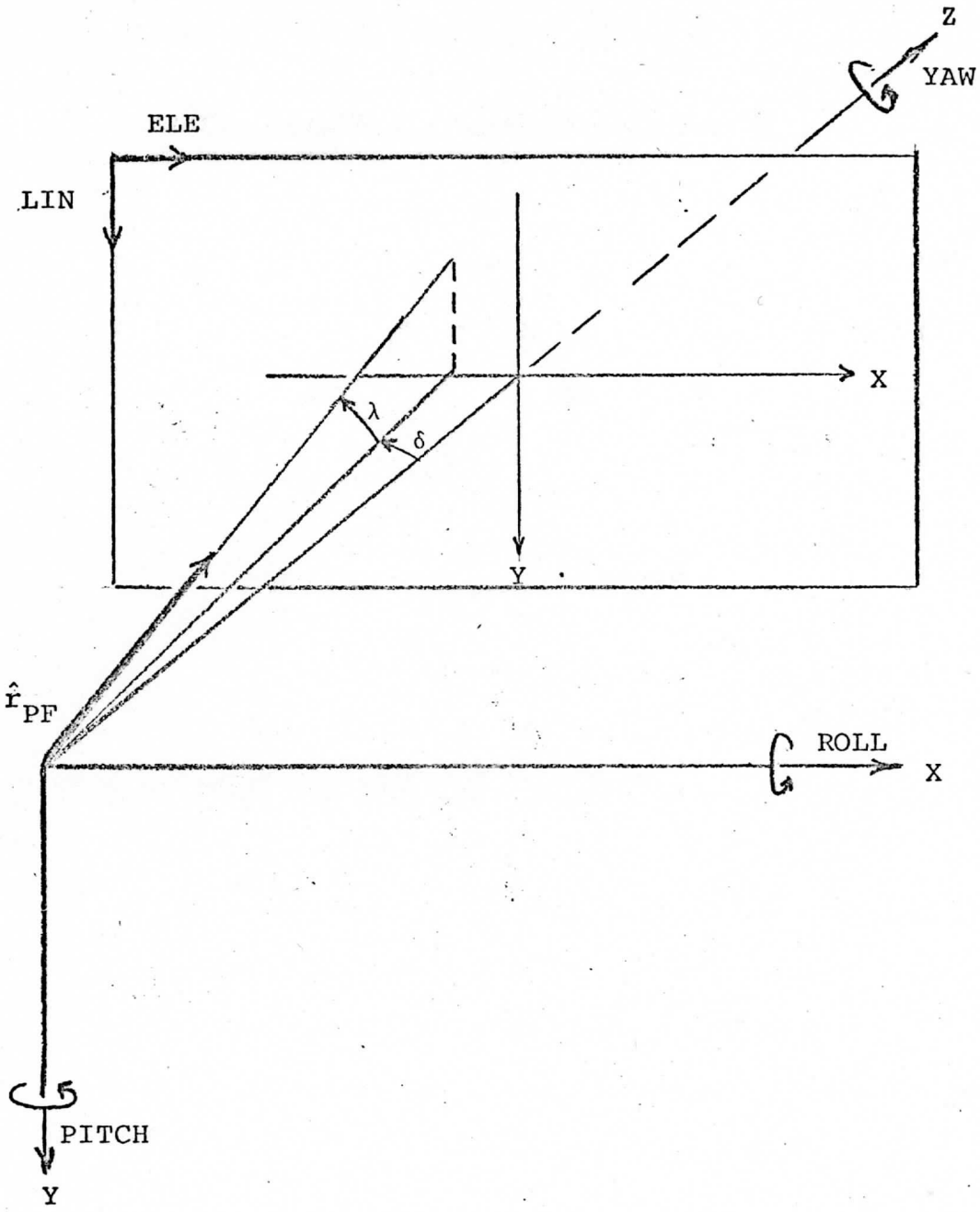

Figure 2. Picture Frame (PF) Coordinate System
(See Text for explanation of symbols)

image frame scan. (For ATS-6, one complete image scan consists of 1200 mirror scans with 2400 samples or elements per scan line.) The PF x-axis is parallel to the center mirror sweep scan at the picture center and nominally points east.

B. Convention for Orthogonal Matrices

Two basic orthogonal transformation representations in transforming a vector from one coordinate system to another with common origin are given here. Their forms arise naturally in the development of the navigation model depending on convenience or available information.

Given two coordinate systems with a common origin whose axes are unprimed xyz and primed x'y'z' respectively, let R represent the orthogonal transformation of the vector $\vec{r}$, (whose components are expressed in the unprimed system) to the vector $\vec{r}'$ whose components are expressed in terms of the primed system, i.e. $\vec{r}' = R\vec{r}$.

The first form R can take is, in matrix representation, $R = [\hat{x}|\hat{y}|\hat{z}]^T$, where $\hat{x}$, $\hat{y}$, $\hat{z}$ are the unit column vectors of the primed coordinate axes whose components are expressed in the unprimed coordinate system. The "T" refers to the transpose of the matrix. To see that this transformation is valid, one need only to carry out the operation implied,

$$\vec{r}' = [\hat{x}|\hat{y}|\hat{z}]^T\vec{r} = (\hat{x}\cdot\vec{r},\ \hat{y}\cdot\vec{r},\ \hat{z}\cdot\vec{r})^T .$$

Thus, $\hat{x}\cdot\vec{r}$, $\hat{y}\cdot\vec{r}$, $\hat{z}\cdot\vec{r}$ represent the projections of $\vec{r}$ onto the x', y', z' axes respectively. This is precisely the representation of $\vec{r}$ in the primed system.

The second form of R is expressed in terms of rotation angles where in its simplest form $R = R(\theta,k)$ represents a rotation by an angle θ counter-

clockwise about the k-th axis as viewed from above where k=1,2,3 refers respectively to the x,y,z-axes. Thus, using the conventions defined above, if the z and z' axes were coincident and the x'y'z' system were rotated by an angle θ counterclockwise relative to the xyz system about the z-axis,

$$\vec{r}' = R(\theta,3)\vec{r} = \begin{bmatrix} \cos\theta & \sin\theta & 0 \\ -\sin\theta & \cos\theta & 0 \\ 0 & 0 & 1 \end{bmatrix} \vec{r} \ .$$

In general for $R(\theta_K,k)$,

$$R_{ki} = R_{ik} = \begin{cases} 0 \text{ if } i \neq k \\ 1 \text{ if } i = k \end{cases} ; \ R_{ii} = \cos\theta, \ i\neq k; \ R_{ij} = -R_{ji} = \sin\theta, \quad i < j \text{ and } i,j\neq k \ .$$

With this notation, the sequence of Euler rotations can be represented in a compact form. For example, the three rotations about the ATS-6 body axes to define the ATS-6 attitude relative to the LV coordinate system are, in sequence, a ccw rotation by an angle θ_y about the BC z-axis (yaw), followed by a ccw rotation by an angle θ_r about the BC x-axis (roll), followed by a cw rotation by an angle θ_p about the BC y-axis (pitch). Thus a vector expressed in the LV system $\vec{r}_{LV}$, is transformed to the BC system ($\vec{r}_{BC}$) by the operation:

$$\vec{r}_{BC} = R(-\theta_p,2)\ R(\theta_r,1)\ R(\theta_y,3)\ \vec{r}_{LV} \ ,$$

where the angles θ_y, θ_r, θ_p are generally dependent on time.

C. Orbit Methods Used in Predicting Satellite Position, $\vec{r}_s(t)$

The orbit parameters used in the model are derived from the ephemeris data available from the ATS-6 magnetic tapes. These data are in the form of position ($\vec{r}_s$) and velocity ($\dot{\vec{r}}_s$) components expressed in the EI coordinate system approximately every three seconds of ephemeris time. For a two body

orbit, a position and velocity vector at any time is theoretically sufficient to uniquely determine the orbit. However, the velocity vectors, unlike the position vectors, are not given with sufficient accuracy for the purposes of this model. Therefore, a Gaussian orbit determination method is used in which two position vectors at different times are used to calculate an accurate velocity vector corresponding to one of the selected position vectors. In symbols,

$$\vec{r}_s(t_1), \vec{r}_s(t_2) \rightarrow \vec{r}_s(t_1), \dot{\vec{r}}_s(t_1), \quad t_1 \neq t_2 .$$

The vector spread between $\vec{r}_s(t_1)$ and $\vec{r}_s(t_2)$ must be less than 70°. Once $\vec{r}_s(t_1)$, $\dot{\vec{r}}_s(t_1)$ are determined, the satellite's position for any other time is determined by an iterative f, g computational procedure:

$$\vec{r}_s(t) = f\,\vec{r}_s(t_1) + g\,\dot{\vec{r}}_s(t_1) .$$

The details of the computational algorithms for these two procedures are given elsewhere.† A thorough testing of these two routines which are incorporated into the ATS-6 model has indicated that any errors generated by them or by uncertainties in the satellite's position are negligibly small compared to errors arising from other sources.

II. THE NAVIGATION MODEL

A. Earth Coordinates to Satellite Image Coordinates

Let t be the instant at which a point on the earth (landmark) is imaged by the satellite scanning system and let $\vec{r}_1(t)$ be the vector which points from the satellite-center to the landmark in question. The relation

---

†P. R. Escobal, Methods of Orbit Determination, J. Wiley and Sons, New York, 1965. Gaussian orbit algorithm, pp. 196-197, f, g method, p. 423.

of this vector to the satellite radius vector $\vec{r}_s$ and the landmark $\vec{r}_2$ is given by:

$$\vec{r}_1(t) = \vec{r}_2(t) - \vec{r}_s(t) \ , \qquad (1)$$

where $\vec{r}_2$, $\vec{r}_s$, and therefore $\vec{r}_1$, are expressed in EI coordinates (Figure 1). The position of the satellite $\vec{r}_s(t)$ is determined from the orbit routine discussed above, while $\vec{r}_2$ is derived as follows:

$$\vec{r}_2 = R(-\theta_E, 3)\ \vec{r}_E \ , \qquad (2)$$

where $\vec{r}_E = \rho(\cos\theta_L \cos\phi_L,\ \cos\theta_L \sin\phi_L,\ (1 - e^2)\sin\theta_L)^T$,

$\rho = r_{eq}/\sqrt{1 - e^2\sin^2\theta_L}$,

θ_L, ϕ_L = the geodetic latitude and longitude of the landmark,

e = eccentricity of the oblate spheriod earth model = 8.1812×10^{-2} ,

r_{eq} = earth's equatorial radius = 6378.15 km.

The landmark $\vec{r}_E$ expressed in ER coordinates is transformed into the EI coordinate system via the transformation $R(-\theta_E, 3)$ where, θ_E, the angle between the x-axes of the two systems at time t is given by

$$\theta_E = a_1 + a_2 * DDD + a_3 * t$$

where, θ_E is the sidereal time of the Greenwich prime meridian,

DDD is the day of the year,

t is universal time,

a_1, a_2, a_3 are constants derived for a specific Julian date; for January 0, 1974

a_1 = 99.59477026 degrees

a_2 = .985647336 degrees/DDD

a_3 = .2506844773 degrees/decimal minute.

It is convenient at this stage to transform the pointing vector $\vec{r}_1$ into a unit vector, $\hat{r}_1(t) = \vec{r}_1(t)/\|\vec{r}_1(t)\|$. Transformation of $\hat{r}_1$ into the LV frame is accomplished by R_{LV},

$$\hat{r}_{LV} = R_{LV}\,\hat{r}_1 = [\hat{x}|\hat{y}|\hat{z}]^T\,\hat{r}_1 \tag{3}$$

where, from the definition of the LV coordinate system,

$$\hat{z} = -\vec{r}_s(t)/\|\vec{r}_s(t)\| = -(x_s, y_s, z_s)^T,$$

$$\hat{x} = (\hat{z} \times \hat{e}_3)/\|\hat{z} \times \hat{e}_3\| = (-y_s/d,\ x_s/d,\ 0)^T,$$

$$\hat{y} = \hat{z} \times \hat{x} = (x_s z_s/d,\ y_s z_s/d,\ -d^2)^T,$$

$$d = \sqrt{x_s^2 + y_s^2},$$

where $x_s^2 + y_s^2 + z_s^2 = 1$.

In matrix form,

$$R_{LV} = \frac{1}{d} \cdot \begin{bmatrix} -y_s & x_s & 0 \\ x_s z_s & y_s z_s & -d^2 \\ -dx_s & -dy_s & -dz_s \end{bmatrix}.$$

Transformation of $\hat{r}_{LV}$ into the BC frame is accomplished by using the properly filtered and estimated attitude angles at time t,

$$\hat{r}_{BC} = R_{BC}\,\hat{r}_{LV}, \tag{4a}$$

$$\text{where } R_{BC} = R(-\theta_p(t), 2)\ R(\theta_r(t), 1)\ R(\theta_y(t), 3), \tag{4b}$$

and θ_p, θ_r, θ_y are the pitch, roll and yaw angles as defined in Part I.B.

The transformation of $\hat{r}_{BC}$ into the image frame vector, $\hat{r}_{PF}$, is

$$\hat{r}_{PF} = (x_{PF}, y_{PF}, z_{PF})^T = R_{PF}\,\hat{r}_{BC}, \tag{5a}$$

$$\text{where } R_{PF} = R(\bar{\theta}_p, 2)\ R(\bar{\theta}_r, 1)\ R(\bar{\theta}_y, 3), \tag{5b}$$

and $\bar{\theta}_y$, $\bar{\theta}_r$, $\bar{\theta}_p$ are the optimized angles resulting from the least-squares navigation technique employing landmark measurements discussed in Section IV of this report. Since R_{PF} is the transformation from the satellite's body-centered frame to its picture (image) frame, it is expected that this transformation will be reasonably time-independent. The effect of thermal and mechanical stresses on the stability of $\bar{\theta}_y$, $\bar{\theta}_r$, $\bar{\theta}_p$ over a period of time on the order of days is something that can only be deduced indirectly by updating the navigation.

With $\hat{r}_{PF}$ determined from equations (5a) and (5b), the satellite image coordinates can be calculated

$$LIN = L_c + (\sin^{-1} y_{PF})/\rho_L, \tag{6a}$$

$$ELE = E_c + (\tan(x_{PF}/z_{PF}))/\rho_E, \tag{6b}$$

where,

LIN = line number,

ELE = element number,

L_c = picture center line = 1200 for visible, 600 for IR ATS-6 image data,

E_c = picture center element = 1200 for ATS-6 image data,

ρ_L = number of radians/line

ρ_E = number of radians/element

} nominal ATS-6 scanned field is $20° \times 20°$.

Summarizing equations (1) - (5),

$$\hat{r}_{PF} = R_{PF}\, R_{BC}\, R_{LV}\, \hat{r}_1, \tag{7a}$$

where $\hat{r}_1 \cdot \|\vec{r}_1\| = \vec{r}_2(t) - \vec{r}_s(t) = R(-\theta_E, 3)\, \vec{r}_E - \vec{r}_s(t)$. (7b)

Equations (7a) and (7b) effectively define the earth coordinates to satellite image coordinates-transformation.

B. Satellite Image Coordinates to Earth Coordinates

For a given LIN, ELE, it is apparent from equations (6) and Figure 2 that

$$\hat{r}_{PF} = (-\cos\lambda\sin\delta,\ -\sin\lambda,\ \cos\lambda\cos\delta)^T \tag{8a}$$

where

$$\lambda = (L_c - LIN)\,\rho_L = \text{mirror step angle} \tag{8b}$$

$$\delta = (E_c - ELE)\,\rho_E = \text{mirror sweep angle.} \tag{8c}$$

From equation (7a),

$$\hat{r}_1 = R_{LV}^T\, R_{BC}^T\, R_{PF}^T\, \hat{r}_{PF} . \tag{9}$$

(The three successive transformations in equation (9) are orthogonal matrices; therefore the inverse of each is equal to its transpose).

Now
$$\vec{r} = \vec{r}_s + s\hat{r}_1 , \tag{10}$$

where $s = \|\vec{r}_1(t)\|$ equals the distance from the satellite-center to the landmark. The solution of s is achieved by using eq. (10) and the equation of the earth spheroid,

$$(x_E^2 + y_E^2)/r_{eq}^2 + z_E^2/r_p^2 = 1 \tag{11}$$

where,

r_{eq} = earth's equatorial radius = 6378.15 km,

r_p = earth's polar radius = 6356.77 km,

x_E, y_E, z_E are the vector components of the landmark, $\vec{r}_E$, in the ER frame.

Equations (2), (10) and (11) represent a system of equations of four unknowns (x_E, y_E, z_E, s). The solution of s can easily be accomplished as follows:

Divide the x and y components by r_{eq} and the z component by r_p in (10).

This results in the equation,

$$\vec{r}_2^{\,*} = \vec{r}_s^{\,*} + s\vec{r}_1^{\,*} \tag{12}$$

where,

$$\vec{r}_2^{\,*} = R(-\theta_E,3)\ \vec{r}_E^{\,*} = R(-\theta_E,3)(x_E/r_{eq}, y_E/r_{eq}, z_E/r_p)^T,$$

$$\vec{r}_1^{\,*} = (x_1/r_{eq}, y_1/r_{eq}, z_1/r_p)^T,$$

$$\vec{r}_s^{\,*} = (x_s/r_{eq}, y_s/r_{eq}, z_s/r_p)^T .$$

Now $\| \vec{r}_2^{\,*} \|^2 = \| R(-\theta_E,3) \|^2 \cdot \| \vec{r}_E^{\,*} \| = 1$, since $R(\theta_E,3)$ is an orthogonal matrix, and $\| \vec{r}_E \|^2$ equals the left side of equation (11). Therefore the equation

$$\| \vec{r}_2^{\,*} \| = 1 = \| \vec{r}_s^{\,*} + s\vec{r}_1^{\,*} \| , \tag{13}$$

contains only s as an unknown. The solution of (13), expressed in a form to minimize computational round-off errors, is:

$$s = -(B + \sqrt{RAD})/A^2, \tag{14}$$

where

$$RAD = B^2 - 4AC,$$

$$A = F + (1 - F)\, z_1^{\,2},$$

$$B = = 2(x_1 x_s + y_1 y_s)\, F + 2 z_1 z_s,$$

$$C = (x_s^2 + y_s^2)\, F + z_s^2 - r_p^2,$$

$$F = r_p^2/r_{eq}^2 .$$

With the solution of s, it follows from (1) and (10) that

$$\vec{r}_E = R(\theta_E,3)(\vec{r}_s + s\hat{r}_1) = (x_E, y_E, z_E)^T, \tag{15}$$

and hence

$$\theta_L = \tan^{-1}[z_E/((1 - e^2)\sqrt{x_E^2 + y_E^2})], \tag{16a}$$

$$\phi_L = \tan^{-1}[y_E/x_E], \tag{16b}$$

where

θ_L = geodetic latitude,

ϕ_L = longitude

$e^2 = (r_{eq}^2 - r_p^2)/r_{eq}^2$ = earth's eccentricity squared.

Equations (9), (15), and (16) constitute the basic - satellite image coordinates to earth coordinates - transformation.

C. Navigation Optimization Procedure

Navigation of the satellite image data base consists of finding a time dependent transformation to predict the earth coordinates from the associated satellite image coordinates. This is accomplished by using landmark measurements from the data base and the model discussed above to determine the optimal transformation in a least-squares sense. A landmark measurement consists of the earth coordinates, (θ_L,ϕ_L), the associated image coordinates, (LIN,ELE), and the time, t, at which the landmark was imaged.

Let

α_i = i^{th} parameter to be optimized,

$R_A(\alpha_i)$ = transformation associated with the α_i,

$\hat{r}_k'$ = unit pointing vector of the k^{th} landmark derived from $(\theta_L,\phi_L)_k$,

$\hat{r}_k$ = unit pointing vector of the k^{th} landmark derived from $(LIN,ELE)_k$,

and

$$S(\alpha_i) = \sum_k \|\hat{r}_k - R_A(\alpha_i)\ \hat{r}_k'\|^2 \tag{17}$$

which is a sum over all landmark measurements included in the optimization. The navigation is complete when a set of parameters α_i are found (call

them $\bar{\alpha}_i$) which minimizes S. The optimized values $\bar{\alpha}_i$ are then used in the transformation to predict (θ_L, ϕ_L) from an arbitrary (LIN,ELE).

As an example, consider equation (5a),

where $$\hat{r}_{PF} = R_{PF}\, \hat{r}_{BC}$$

and let us assume that the attitude telemetry data is known with a reasonable degree of accuracy but that the orientation of the PF frame relative to the BC frame is not. Thus, we wish to optimize θ_y, θ_r, θ_p in the transformation R_{PF}. Using the landmark measurements and the attitude telemetry data, calculate $\hat{r}_{BC}$ as given by equations (1) to (4a) and $\hat{r}_{PF}$ from equations (8) for each landmark; therefore S in this case takes the form

$$S(\theta_y,\theta_r,\theta_p) = \sum_k \| (\hat{r}_{PF})_k - R_{PF}(\theta_y,\theta_r,\theta_p)(\hat{r}_{BC})_k \|^2,$$

and the values $\bar{\theta}_y$, $\bar{\theta}_r$, $\bar{\theta}_p$ which minimize S are the ones then used in equation (5b).

The method used to minimize $S(\alpha_i)$ is an iterative procedure which uses a modified Newton's method.

Let

α = $\{\alpha_i\}$ for convenience,

α^n = value of α resulting from the n^{th} iteration,

N = total number of parameters α_i,

H = N × N matrix (Hessian) whose ij^{th} component is $[H]_{ij} = \partial^2 S/\partial\alpha_i \partial\alpha_j$,

∇S = gradient of S, $(\nabla S)_i = \partial S/\partial\alpha_i$.

The iterative procedure works as follows:

1) Start with m = 0 and increase m by 1 until a value M is found such that

$$S(\alpha^n) - S(\alpha^n - 2^{-M} H^{-1}\nabla S(\alpha^n)) \geq (.4)2^{-M} H^{-1}\nabla S(\alpha^n) \cdot \nabla S(\alpha^n),$$

2) When the inequality is satisfied, set

$$\alpha^{n+1} = \alpha^n - 2^{-M} H^{-1}\nabla S(\alpha^n),$$

3) Check to see if the following convergence criteria is met

$$|S(\alpha^{n+1}) - S(\alpha^n)| \leq 10^{-18}|S(\alpha^n)| .$$

If no, set $\alpha^n \leftarrow \alpha^{n+1}$ and go to 1); if yes, then $\alpha^{n+1} = \bar{\alpha}$ and the procedure is finished.